Research Article Vol. 33, No. 19 / 22 Sep 2025 / Optics Express 40969
Optics EXPRESS

Comprehensive theoretical model for multi-harmonic dispersion-tuned mode-locking (DTML) for use in swept-source OCT

RENE RIHA,* ALEJANDRO MARTINEZ JIMENEZ, AND ADRIAN PODOLEANU

Applied Optics Group, University of Kent, School of Physical Sciences, Canterbury, Kent, CT2 7NH, UK
rr406@kent.ac.uk

Abstract: In this study, a comprehensive theoretical model for the multi-harmonic dispersion-tuned mode-locking (DTML) regime for swept-source OCT (SS-OCT) is presented for the first time. The principle of wavelength tuning in this regime is described in detail, along with a derivation of the tuning bandwidth formula and scaling guidelines that predict the trade-offs between the tuning bandwidth and coherence performance. A comparison of the optical fields stored inside a conventional single-harmonic DTML cavity, a multi-harmonic DTML cavity, and an FDML cavity is also presented. As experimental validation of the multi-harmonic concept, OCT images of a finger tip and the retina of a volunteer are captured at a sweep rate close to 1 MHz with a 30 nm tuning bandwidth.

1. Introduction

Optical coherence tomography (OCT) has evolved as a highly relevant high resolution imaging method in ophthalmology, cardiology, and dermatology [1,2]. The key parameters defining OCT performance include depth resolution, imaging depth range, acquisition speed, sensitivity, and sensitivity roll-off with depth. One of the OCT methods that in the last decade has proven MHz acquisition rate is the swept source (SS)-OCT [3,4]. This enables not only a high speed, but a longer imaging depths than in the spectrometer-based OCT methods.

Two main types of swept sources are used in SS-OCT systems [3]. The first type relies on mechanical movements, which can be implemented by actuating on the mirrors of a Fabry-Perot (FP) filter in a Fourier-domain mode-locked (FDML) laser [5], or using a polygon mirror scanner [6], or a micro-electromechanical system vertical-cavity surface-emitting laser (MEMS-VCSEL) [7]. The second type employs akinetic tuning principles, based on an acousto-optic deflection [8], or all-semiconductor designs [9], or time-stretch technology [10], or stretched-pulse mode-locking (SPML) [11], or dispersion-tuned mode-locking (DTML) [12].

FDML, SPML, and DTML swept sources, with cavity lengths ranging from several meters to kilometers, are typically categorized as long-cavity lasers [3]. In such lasers, thousands of optical modes lie within the gain bandwidth. In FDML, wavelength selection is governed by an intracavity tunable element (an FP filter). In DTML, a combination of a mode-locking with a dispersive element enables tuning. These operating principles are fundamentally different from that of short-cavity lasers, such as MEMS-VCSELs, whose cavity length is only a few micrometers and therefore supports a single optical mode only. In MEMS-VCSELs, wavelength tuning is obtained by actuating the MEMS mirror to alter the cavity length. This motion induces a Doppler shift at each reflection, resulting in an adiabatic frequency shift of the lasing mode [3].

A DTML laser comprises three main elements: a gain medium, typically a semiconductor optical amplifier (SOA), a mode-locking element, based on the direct modulation of the SOA

#569516 https://doi.org/10.1364/OE.569516
Journal © 2025 Received 6 Jun 2025; revised 6 Sep 2025; accepted 9 Sep 2025; published 18 Sep 2025

Optics EXPRESS

gain or employing an external intensity modulator, and a dispersive element, realized either by a long optical fiber or a chirped fiber Bragg grating (cFBG). In a standard *single-harmonic* DTML laser, active mode-locking is applied at a single harmonic order. Desirable emission properties from this laser configuration include satisfactory power and a sufficiently long coherence length, which can be achieved by a combination of a relatively short cavity length (units of meters), a narrow temporal modulation window (below 100 ps), and a high level of dispersion (preferably over $\gtrsim$ 10 ps/nm). Three generations of single-harmonic DTML lasers can be identified. The 1st generation employed extended pieces of fiber ($\sim$ 100 – 1000 m) as the dispersive element [13]. By using long fiber cavities, sweep rates of only a few kHz were achievable. In the 2nd generation, a cFBG was employed as the dispersive element [14], significantly reducing the cavity length that enabled larger sweep rates of tens of kHz. In the 3rd generation, the direct modulation of the SOA gain inducing mode-locking was replaced with modulation via a high speed intensity modulator [12]. This modification allowed the gain medium to operate under a more stable operation. In addition, as intensity modulators are available with over tens of GHz electrical bandwidth, subnanosecond modulation temporal windows became accessible, which are unachievable when modulating the SOA. By using narrow window pulse modulation instead of sinusoidal modulation, coherence of the laser is improved [12,15]. Single-harmonic DTML swept sources have been demonstrated across various wavelengths of interest to OCT, spanning over 850 nm [13,16], 1 μm [12], 1.3 μm [13,14], and 1.55 μm [13,15].

In the previous reports published by our group [17–19], it was demonstrated that an alternative sweeping regime can be established inside a DTML laser. This regime, involving two simultaneous "resonant" conditions, was initially referred as to the *dual resonance sweeping regime* or *dual resonance DTML*. The first resonant condition corresponds to active mode-locking (achieved via the direct modulation of the SOA gain or an external modulator) at a harmonic of the fundamental frequency of the cavity. The second resonant condition is inspired by the Fourier-domain mode-locking (FDML) technology [20], where the mode-locking element (typically a Fabry-Perot filter) is driven at the cavity fundamental frequency. When both resonant conditions are applied to a DTML cavity, it is observed that, contrary to FDML, wavelength tuning does not occur if the sweep rate precisely matches the fundamental frequency. Instead, only a single wavelength emission appears at the output of the DTML laser. It is experimentally observed that wavelength tuning is achieved if the sweep rate is actually slightly detuned from the fundamental frequency [17–19]. For the first time, the presented study provides a rigorous theoretical explanation for this behavior. Because multiple orders of harmonics are engaged, a more accurate reference to this regime is proposed in this study, as to the *multi-harmonic DTML*. This regime is fundamentally different from the standard single-harmonic mode-locking presented by all other research groups in the field of DTML swept sources.

The multi-harmonic DTML regime has previously been demonstrated at 850 nm [17] and 1550 nm [18] using direct modulation of the SOA gain. Later, an improved operation was demonstrated at 1550 nm by using an external intensity modulator [19]. This has led to both extended tuning bandwidth and increased coherence length compared to the the direct modulation of the SOA. The previous reports reduced to presenting primarily experimental demonstrations. However, a comprehensive theoretical description of the multi-harmonic operation, discussion on its tuning and coherence performance, its demonstration at 1 μm, and finally actual OCT images produced by employing this regime have not been reported so far.

In this study, the principle of wavelength tuning in this regime is described in detail by examining the relationship between the spectral content of the modulation signal and the optical spectrum of the laser. A spectral filtering framework is employed to identify scaling guidelines that predict the trade-offs between the tuning bandwidth and coherence performance. The developed theoretical model reveals important similarities with the FDML regime, which we hope will make interesting reading for laser physics specialists. In addition to a detailed description

Optics EXPRESS

of the multi-harmonic regime and its performance trade-offs, this study demonstrates the first implementation of a multi-harmonic DTML swept source operating at 1 μm. By employing a cFBG as the dispersive element and short 50 ps modulation windows, wavelength tuning across a 30 nm bandwidth at a 944 kHz sweep rate is achieved in a 200 m fiber cavity. Furthermore, when integrated into an OCT interferometer, an imaging depth of 1 mm and a sensitivity of 90 dB are achieved. Owing to its coherence and high signal-to-noise performance of the laser, OCT images of a finger tip and the retina of a volunteer are captured at a sweep rate close to 1 MHz.

2. Methods

The DTML swept source (DTML-SS) researched is schematically depicted in Fig. 1. Gain in the cavity is provided by a semiconductor optical amplifier (SOA, Innolume SOA-1060-90-PM-30dB, maximum gain bandwidth 90 nm), whilst dispersion is produced by a chirped fiber Bragg grating (cFBG, Teraxion PSR-1040-200(+21.9-0.046)-0S2-0L, dispersion 22 ps/nm, bandwidth 200 nm). Mode-locking in the cavity is achieved by employing an intensity modulator (IM, Optilab IMP-1064-20-PM, electronic bandwidth 20 GHz, optical bandwidth 60 nm). Through an optical circulator (CIRC, OZ Optics FOC-12P-111-6/125-PPP-1060-50-3A3A3A-1-1-WB, bandwidth 100 nm), the light is directed to the cFBG, and 20% of the power is coupled out through its transmission end. A 100 m fiber delay is inserted between the CIRC and the cFBG, providing an additional 200 m to the cavity length. After transmission through an isolator (ISO, AFW ISOS-64-B-1-2), the output light is amplified through a booster amplifier (BOA, Innolume BOA-1060-80-HI-120mW, maximum gain bandwidth 80 nm). The fundamental frequency of the cavity is evaluated to be 944 kHz, corresponding to a total cavity round-trip length of 217 m, and the cavity dispersion is estimated to be 14.3 ps/nm using the evaluation technique described in [21].

A schematic diagram of the signal generator driving the IM is depicted in Fig. 1 in the green dashed box. A voltage-controlled oscillator (VCO, Mini-Circuits ROS-3000-819+), is driven by DC voltage (V_{DC}) from a regulated power supply (PS) and AC voltage ($V_{AC}(t)$) from a signal generator (SG, Agilent Technologies 81160A). The VCO produces a sinusoidal wave signal $V(t)$ with a frequency $f(t)$ proportional to V_{DC} and $V_{AC}(t)$,

$$f(t) = \eta_{VCO}[V_{DC} + V_{AC}(t)], \tag{1}$$

where η_{VCO} is the Hz/V tuning sensitivity. A VCO instead of a professional signal generator is employed here for its large RF bandwidth that it can provide (units of GHz). Such a large RF bandwidth is necessary for the multi-harmonic DTML, where many mode-locking harmonic orders are engaged. In addition, VCOs are generally of significantly lower cost and more compact size than professional signal generators. As a trade-off, due to the large ratio between its bandwidth and central frequency, the VCO tuning sensitivity $\eta_{VCO} = \eta_{VCO}(V_{DC}, V_{AC}(t))$ may not be precisely constant over a large range of input voltages. The VCO signal is then directed to a pulse generator (PG, AlnairLabs EPG-210M-0050-S-P-N-N), which generates a short pulse of 50 ps width per each period of the input sinusoidal signal. This means that the pulse repetition frequency f is that of the instantaneous input sinusoidal signal provided by the VCO. The pulses are then amplified up to 5 V peak-to-peak amplitude with a negligible distortion through a pair of cascaded RF amplifiers (RFA, Mini-Circuits ZVA-01243+, 1 − 22 GHz, 22 dBm, and Xmicrowave XM-A3E6-0804C-01, DC-20 GHz, 25 dBm) and applied to the IM. Finally, the bias of the IM is controlled separately by a DC voltage (V_{bias}) from a second output of the PS.

The experimental OCT setup driven by the multi-harmonic DTML-SS is displayed in Fig. 2. The interferometer comprises two couplers, with a recirculation path in the reference arm to prevent the light being directed back into the swept source. In the object arm, 20% of the coupled light is deflected by a system of two galvanometer scanning mirrors. The interferometer is terminated on a balanced photodetector block (bPhD, Thorlabs PDB481C-AC). A 12-bit

Optics EXPRESS

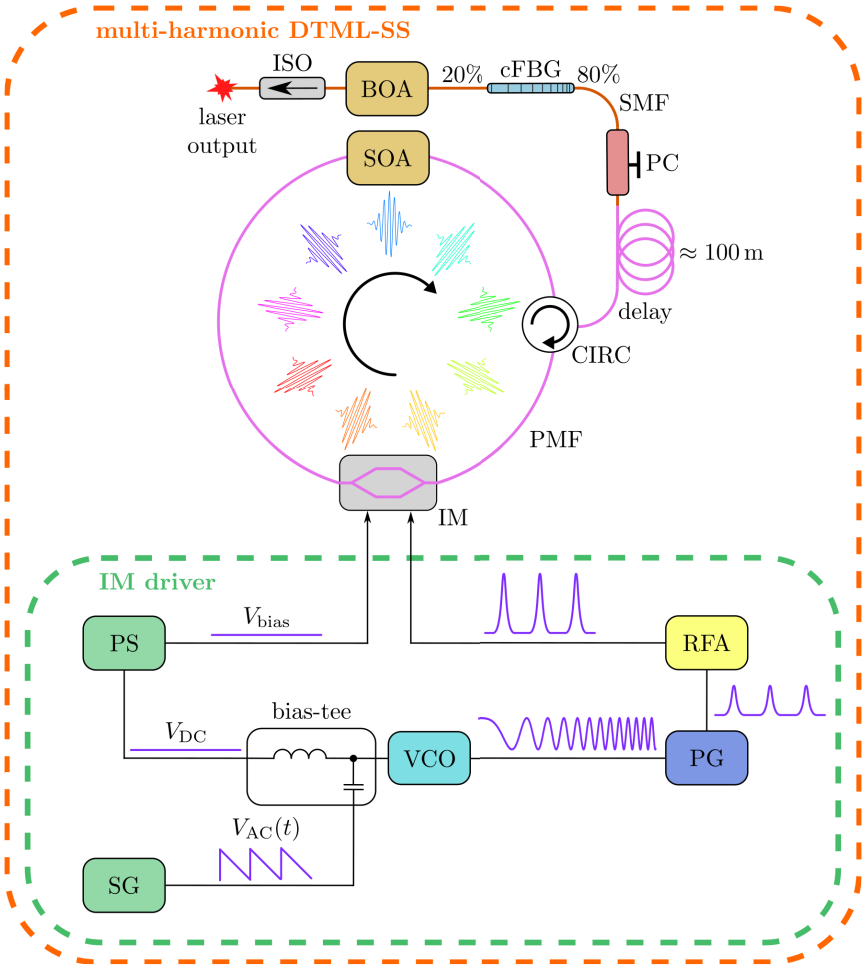

Fig. 1. DTML-SS. SOA: semiconductor optical amplifier, CIRC: circulator, PC: polarization controller, SMF: single mode fiber, cFBG: chirped fiber Bragg grating, ISO: isolator, BOA: booster amplifier, IM: intensity modulator, PMF: polarization maintaining fiber, PS: power supply, SG: signal generator, VCO: voltage-controlled oscillator, PG: pulse generator, RFA: RF amplifier, V_{DC}: DC voltage, $V_{\mathrm{AC}}(t)$: AC voltage, V_{bias}: IM bias voltage. f_{cav} denotes the fundamental frequency of the cavity. The fundamental frequency of the cavity is evaluated to be 944 kHz.

waveform digitizer board samples the photodetected signal at a rate of 4 GS/s (AlazarTech ATS9373). Using the Complex Leader-Follower (CLF) interferometry method [22–24], A-scan and B-scan OCT images are obtained.

2.1. Standard single-harmonic DTML

2.1.1. Principle of wavelength tuning

The principle of DTML is based on active mode-locking inside a dispersive cavity [25]. Due to chromatic dispersion, the longitudinal modes at which lasing can occur are spaced unevenly, with the spacing given by the wavelength-dependent fundamental frequency of the cavity $f_{\mathrm{cav}}(\lambda)$. For a fiber ring cavity consisting of a fiber delay of length L_{fiber} and a cFBG of length $L_{\mathrm{cFBG}}(\lambda)$,

Optics EXPRESS

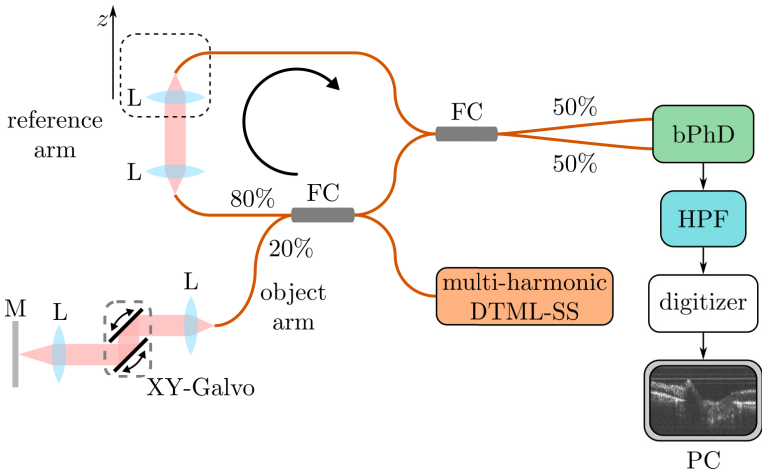

Fig. 2. OCT setup. FC: fiber coupler, L: lens, M: mirror, bPhD: balanced photodetector block, HPF: high pass filter. The recirculation of the light in the reference arm is labeled with the bent arrow.

as depicted in Fig. 1, $f_{\mathrm{cav}}(\lambda)$ can be generally expressed as [26]:

$$f_{\mathrm{cav}}(\lambda) = \frac{c}{n_{\mathrm{g}}(\lambda)L_{\mathrm{fiber}} + n_{\mathrm{g}}(\lambda_0)L_{\mathrm{cFBG}}(\lambda)}, \tag{2}$$

where c is the speed of light and $n_{\mathrm{g}}(\lambda)$ is the group index of refraction of the fiber. The wavelength-dependent contributions to the overall cavity dispersion originating in the fiber delay and cFBG are contained in $n_{\mathrm{g}}(\lambda)$ and $L_{\mathrm{cFBG}}(\lambda)$, respectively. In practical DTML implementations, it can be assumed that $D_{\mathrm{cFBG}}/D_{\mathrm{fiber}} \sim 10^4$-$10^5$, where D_{cFBG} and D_{fiber} denote the dispersion coefficients with units of $\mathrm{s/m^2}$ originating in the Bragg grating and fiber material, respectively. This means that the dispersion contribution from the fiber material over the cFBG length can be neglected. Therefore, in comparison with the formula for $f_{\mathrm{cav}}(\lambda)$ in [26], the form (2) expressed here is slightly modified by considering the index of refraction of the cFBG as $n_{\mathrm{g}}(\lambda) = n_{\mathrm{g}}(\lambda_0)$. This approximation will simplify the following mathematical treatment, while still adequately describing the general case of a long fiber delay and a cFBG both contributing to the overall cavity dispersion.

To mode-lock the cavity, the losses or gain must be periodically modulated at a modulation frequency f matching an integer multiple q of the fundamental frequency of the cavity $f_{\mathrm{cav}}(\lambda)$,

$$f = q f_{\mathrm{cav}}(\lambda), \tag{3}$$

where q is also called the harmonic order of mode-locking. A graphical representation of the emission wavelength λ as a function of f in Fig. 3 consists of tuning bands, where each band corresponds to a different harmonic order $q = q_{\mathrm{c}} + l$, with q_{c} as the reference harmonic order and l as an integer. To find the relationship between a shift in the emission wavelength $\Delta\lambda_{\mathrm{single}} = \lambda_{\mathrm{end}} - \lambda_{\mathrm{start}}$ within a single harmonic tuning band q and a change in the modulation frequency $\Delta f = f_{\mathrm{end}} - f_{\mathrm{start}}$, the slope $\mathrm{d}\lambda/\mathrm{d}f$ is first obtained by differentiating (3) with respect to

Optics EXPRESS

λ and inverting the result as:

$$\begin{aligned}\frac{\mathrm{d}\lambda}{\mathrm{d}f} &= -\frac{q}{f^2}\left[\frac{L_{\mathrm{fiber}}}{c}\frac{\mathrm{d}n_{\mathrm{g}}(\lambda)}{\mathrm{d}\lambda} + \frac{n_{\mathrm{g}}(\lambda_0)}{c}\frac{\mathrm{d}L_{\mathrm{cFBG}}(\lambda)}{\mathrm{d}\lambda}\right]^{-1} \\ &= -\frac{q}{f^2(\mathrm{TDD}_{\mathrm{fiber}} + \mathrm{TDD}_{\mathrm{cFBG}})} \\ &= -\frac{q}{f^2\mathrm{TDD}_{\mathrm{cav}}},\end{aligned} \tag{4}$$

where TDD denotes the time delay dispersion with units of s/m, and $\mathrm{TDD}_{\mathrm{cav}}$ is the overall cavity dispersion. $\mathrm{TDD}_{\mathrm{cav}}$ generally includes the dispersion contributions from both the fiber, $\mathrm{TDD}_{\mathrm{fiber}} = D_{\mathrm{fiber}}L_{\mathrm{fiber}}$, and the cFBG, $\mathrm{TDD}_{\mathrm{cFBG}} = D_{\mathrm{cFBG}}L_{\mathrm{cFBG}}$ (L_{cFBG} is here the geometrical cFBG length independent of λ). The dispersion relations used in (4) can be found in [25,26]. In the 1st generation of DTML lasers (long cavities with fiber alone contributing to the cavity dispersion), dispersion in the cavity is given by $\mathrm{TDD}_{\mathrm{fiber}}$, while in the 2nd and 3rd generation DTML lasers (short cavity with a cFBG), dispersion in the cavity is dominated by $\mathrm{TDD}_{\mathrm{cFBG}}$ (i.e., $\mathrm{TDD}_{\mathrm{fiber}}$ can be neglected). Apparently, the larger the frequency f in (4), the smaller the slope $\mathrm{d}\lambda/\mathrm{d}f$, as graphically depicted in Fig. 3. Provided a change in the modulation frequency Δf is applied to the modulator, a general expression for $\Delta\lambda_{\mathrm{single}}$ can be obtained by integration of (4) over Δf as shown below:

$$\begin{aligned}\Delta\lambda_{\mathrm{single}} &= \int_{f_0-\Delta f/2}^{f_0+\Delta f/2}\frac{\mathrm{d}\lambda}{\mathrm{d}f}\mathrm{d}f = -\frac{q}{\mathrm{TDD}_{\mathrm{cav}}}\int_{f_0-\Delta f/2}^{f_0+\Delta f/2}\frac{\mathrm{d}f}{f^2} \\ &= -\frac{q}{\mathrm{TDD}_{\mathrm{cav}}}\left(-\frac{1}{f_0+\Delta f/2} + \frac{1}{f_0-\Delta f/2}\right),\end{aligned} \tag{5}$$

with $f_0 \equiv qf_{\mathrm{cav}}(\lambda_0)$. Because all modulation frequencies within Δf in (5) lock the laser at a single qth harmonic order, this mode-locking regime is referred to as the single-harmonic regime. The expression in (5) is applicable for very low harmonic orders cases when the slope $\mathrm{d}\lambda/\mathrm{d}f$ changes significantly within a single tuning band $q = q_{\mathrm{c}} + l$ in Fig. 3. This is the case if some of the very low harmonic orders are employed for DTML [26], which is however an exception in this type of laser used only in cavities with very large dispersion (over 200 ps/nm in [26]). If $f = qf_{\mathrm{cav}}(\lambda) \gg \Delta f/2$, (5) can be approximated by a first order expansion of the terms in the parentheses, leading to a linear relationship commonly found in DTML swept sources literature [12–14,27–30]:

$$\Delta\lambda_{\mathrm{single}} \approx -\frac{1}{\mathrm{TDD}_{\mathrm{cav}}f_{\mathrm{cav}}f_0}\Delta f = S(f_0)\Delta f, \tag{6}$$

where $f_{\mathrm{cav}} \equiv f_{\mathrm{cav}}(\lambda_0)$ represents the effective fundamental frequency of the cavity, and $S(f_0)$ denotes the tuning sensitivity, which generally depends on the cavity dispersion, its length, and central modulation frequency f_0. Considering an anomalous dispersive cavity, i.e., when $\mathrm{TDD}_{\mathrm{cav}}>0$, for $\Delta f>0$, the laser emission is tuned from short to long wavelengths (the forward direction), while for $\Delta f<0$, the emission is tuned from long to short wavelengths (the backward direction). The directions of wavelength tuning are reversed for the case of a normal dispersive cavity, i.e., when $\mathrm{TDD}_{\mathrm{cav}}<0$. In the time domain, the wavelength tuning during the sweep of f arises from a slight temporal delay between a mode-locked chirped pulse (induced by chromatic dispersion) and the modulation window as the pulse passes through the modulator, as described in more detail in [31].

For better comprehension of the advance from the standard single-harmonic to the novel multi-harmonic DTML, it will be helpful to describe the laser optical spectrum in relation to the

Optics EXPRESS

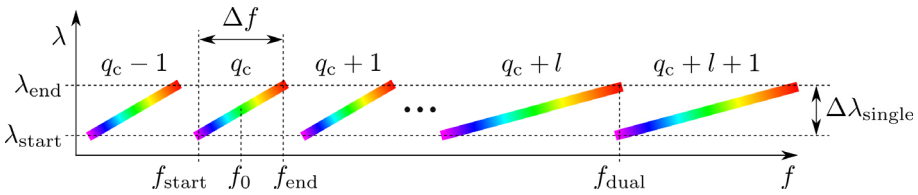

Fig. 3. A graphical representation of the tuning bands $q = q_c + l$ and emission wavelength λ as a function of the modulation frequency f of the signal applied to the intensity modulator. The connection between Δf and $\Delta\lambda_{single}$ is given by (5) or (6).

spectral content of the modulation signal over large number of sweep cycles (periods $T_s = 1/f_s$). Using the properties of the convolution operation $x(t) \circledast y(t)$ and of the Dirac comb $\sum_l \delta(t - l)$ [25], the modulation signal $V(t)$ in Fig. 4 produced by the VCO can be written in the form:

$$V(t) = V_{cycle}(t) \circledast \sum_{l=-\infty}^{+\infty} \delta(t - lT_s). \tag{7}$$

$V_{cycle}(t)$ here represents the single sweep cycle modulation signal inside the red dashed rectangle in Fig. 4:

$$V_{cycle}(t) = \text{rect}\left(\frac{t - T_s/2}{T_s}\right) \sin\left[2\pi \int_0^t f(t')\mathrm{d}t'\right], \tag{8}$$

where a modulation depth of 1 is considered. The rectangular function rect(t) [25] in (8) constraints the $V_{cycle}(t)$ to one period T_s interval, and the integral calculates the time-domain instantaneous phase of the signal. Assuming a linear sweeping with the sweep frequency $f_s = 1/T_s$, $f(t)$ can be represented by a sawtooth shape, as depicted in Fig. 4, according to:

$$f(t) = \Delta f\,(f_s t - \lfloor f_s t + 1 \rfloor) + f_0 + \frac{\Delta f}{2}\text{sgn}\,\Delta f, \tag{9}$$

while still following the relationship between $\Delta\lambda$ and Δf, as given by (5) or (6). $\lfloor x \rfloor$ in (9) denotes the floor function, which rounds a real number x down to the nearest integer. When $\Delta f > 0$, (9) represents a positive sawtooth signal, while when $\Delta f < 0$, (9) describes a negative sawtooth signal. Combining (7)–9, the signal in (7) is constructed by repeating $V_{cycle}(t)$ at a rate f_s, with the modulation frequency varying according to $f(t)$ specified by (9).

Using the Fourier transform properties [25] and omitting multiplicative constants, the spectrum $\widetilde{V}(f)$ of the modulation signal $V(t)$ specified by (7) can be expressed as:

$$\begin{aligned}\widetilde{V}(f) &\sim \widetilde{V}_{cycle}\left(\frac{f - f_0}{\Delta f}\right) \sum_{l=-\infty}^{+\infty} \delta\left(f - lf_s - f_0 + \left\lfloor \frac{f_0}{f_s} \right\rfloor f_s\right) \\ &= \widetilde{V}_{cycle}\left(\frac{f - f_0}{\Delta f}\right) \sum_{l=-\infty}^{+\infty} \delta(f - f_0 - lf_s),\end{aligned} \tag{10}$$

where $\widetilde{V}_{cycle}[(f - f_0)/\Delta f]$ represents the spectral amplitude envelope, $f_0 - \lfloor f_0/f_s \rfloor f_s$ is the frequency comb offset, and f_s is the spacing between the comb frequency components $f_l = f_0 + lf_s$. Note that the envelope is centered around f_0 and that, due to the offset $f_0 - \lfloor f_0/f_s \rfloor f_s$, there is always a comb component at f_0 for $l = 0$, regardless of the value of f_s. To enable sweeping across a large number of tuning bands in Fig. 3 at MHz rates, a VCO with a wide frequency range is required for the multi-harmonic DTML operation. Since a wide range can only be delivered by VCOs oscillating

Optics EXPRESS

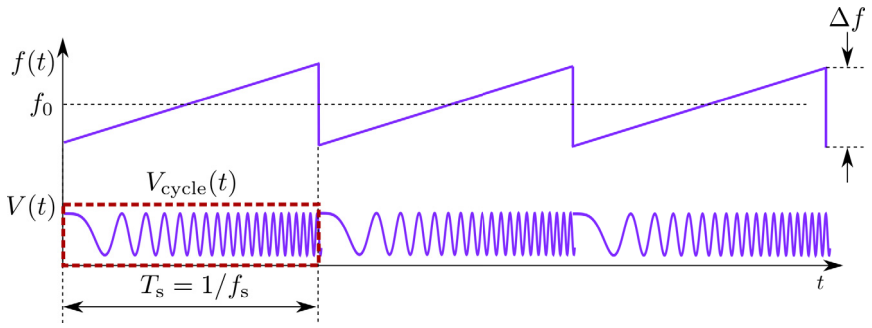

Fig. 4. A graphical representation of the modulation signal $V(t)$ and the modulation frequency $f(t)$ given by (7) and (9), respectively. $V_{\text{cycle}}(t)$: single sweep cycle modulation signal given by (8), T_s: sweep period, f_0: central modulation frequency, Δf: modulation frequency range.

at larger central frequency than the range, ranges on the order of several hundred MHz to GHz are generally only achievable with VCOs operating in the GHz range. The top panel of Fig. 5 shows a simulated spectrum $\widetilde{V}(f)$, corresponding to a time-domain modulation signal $V(t)$ defined by Eqs. (7)–(9). The central frequency of $f_0 = 2330$ MHz and the sweep frequency of $f_s = 1$ MHz are close to those in the experimental section. However, to simplify the simulation, a reduced modulation range of $\Delta f = 100$ MHz is here simulated, in which case a constant sensitivity η_{VCO} in (1) is expected. It can be observed that the frequency extension of $\widetilde{V}(f)$ is approximately equal to Δf, and that the spectrum contains approximately $\Delta f/f_s \approx 100$ frequency components. The experimentally measured spectral content of the VCO signal using an RF spectrum analyzer, for the same parameters, is displayed in the bottom panel of Fig. 5, demonstrating a good agreement with the simulation above. The nature and properties of the comb-like spectra in Fig. 5 are important for the explanation of the multi-harmonic operation principle.

When the laser is mode-locked, the frequency components $f_l = f_0 + lf_s$ given by (10) match the resonant frequencies $q_c f_{\text{cav}}(\lambda_l)$ of the cavity,

$$\begin{aligned} f_l &= f_0 + lf_s = q_c f_{\text{cav}}(\lambda_0) + lf_s \\ &= q_c f_{\text{cav}}(\lambda_l), \end{aligned} \tag{11}$$

where an arbitrary single q_cth tuning band was chosen to simplify the notation. As depicted in the top panel of Fig. 6, each component f_l (vertical blue bars) corresponds to a different emission wavelength λ_l from the single q_cth tuning band. Note that the example of 5 components f_l in the figure and spacing $f_s = f_{l+1} - f_l \ll f_{\text{cav}}$ are not a scale. In the single-harmonic DTML, Δf is not bigger than f_{cav}, and f_s is much smaller than f_{cav}. Considering the total number of frequency components as $\approx \Delta f/f_s + 1$ and assuming a constant tuning sensitivity $S(f_0)$ across the q_cth tuning band, the tuning bandwidth $\Delta\lambda_{\text{single}}$ given by (6) can be expressed alternatively as a sum of fractional bandwidths $\Delta\lambda_{l+1,l} = \lambda_{l+1} - \lambda_l$:

$$\begin{aligned} \Delta\lambda_{\text{single}} &\approx \sum_{l=-\Delta f/2f_s}^{\Delta f/2f_s} \Delta\lambda_{l+1,l} = \sum_{l=-\Delta f/2f_s}^{\Delta f/2f_s} S(f_0) f_s \\ &\approx S(f_0)\frac{\Delta f}{f_s} f_s = S(f_0)\Delta f, \end{aligned} \tag{12}$$

leading to the same result as derived in (6). The laser optical spectrum for the single-harmonic regime is graphically depicted in the middle panel of Fig. 6. Such a spectrum can be observed on an optical spectrum analyzer for an integration time much larger than T_s. The spectrum

Optics EXPRESS

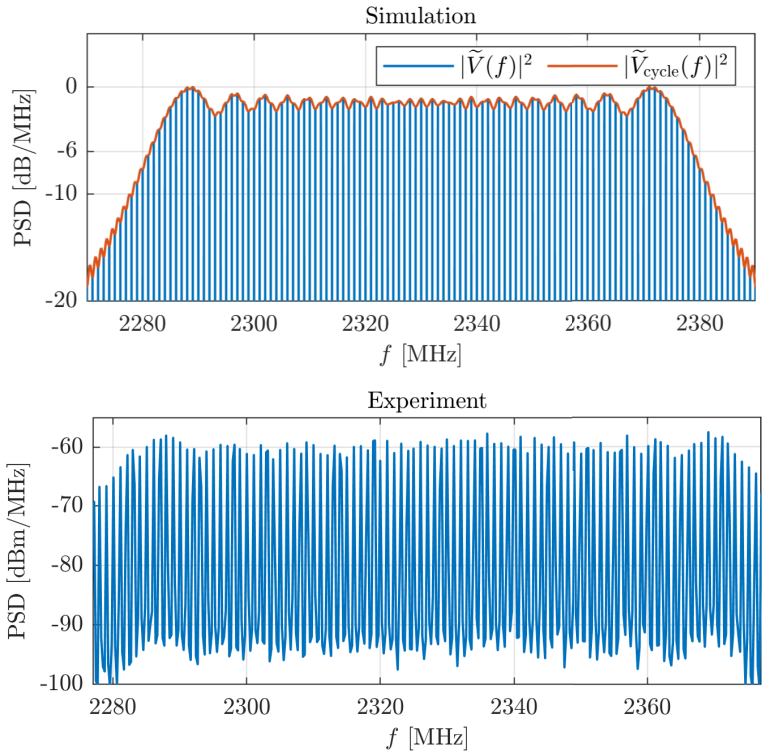

Fig. 5. Top: Simulation of the spectrum of the modulation signal $V(t)$ specified by (7)–10. **Bottom:** Experimentally measured VCO signal for $f_0 \doteq 2330$ MHz, $\Delta f \doteq 100$ MHz, and $f_s \doteq 1$ MHz.

consists of spectral lines with an instantaneous linewidth of $\delta\lambda$ (optical linewidth $\delta\nu = c\delta\lambda/\lambda^2$ in Fig. 6) at wavelengths λ_l (optical frequencies $\nu_l = c/\lambda_l$ in Fig. 6). The exact spectral shape and linewidth of the lines can be evaluated using a perturbed Gaussian or hyperbolic secant function, as follows from mathematical modeling of the cavity components and their effects on pulse propagation inside the cavity in Fig. 1 [15,25,31–33]. For the graphical purposes, the spectral lines in Fig. 6 are approximated by a Gaussian spectral line with a linewidth $\delta\nu$, of which coherence properties will be examined later. In the single-harmonic DTML, the modes within each spectral line (the vertical bars) are locked at the same q_cth harmonic order with spacing given by $\Delta\nu_{m,l} = q_c f_{cav}(\lambda_l)$. Each spectral line represents the spectrum of a monochromatic pulse train with a carrier wavelength λ_l and a pulse rate given by $f_{p,l} = \Delta\nu_{m,l} = q_c f_{cav}(\lambda_l)$, perpetually circulating inside the cavity, as depicted in the bottom panel of Fig. 6. A superposition of these monochromatic trains leads to a pulse train with a carrier wavelength varying over time, shown as snapshots of the optical field inside the cavity at periods of T_s in the bottom panel of Fig. 6.

2.1.2. Tuning bandwidth limitations

Several factors in DTML limit the achievable tuning bandwidth $|\Delta\lambda_{single}|$. An important factor is the gain bandwidth of the employed SOA, and to some extent the optical bandwidths of the other cavity components. Another factor is related to the condition preventing emission from neighboring tuning bands $q_c + l$ and $q_c + l + 1$ in Fig. 3. To prevent the laser from an undesired dual wavelength emission at $f_{dual} = (q_c + l)f_{cav}(\lambda_{end}) = (q_c + l + 1)f_{cav}(\lambda_{start})$, where two wavelengths λ_{end} and λ_{start} are emitted at the same time, the range Δf in (6) should not exceed the fundamental frequency f_{cav}. This condition provides an estimation for the maximum single-harmonic non-dual

Optics EXPRESS

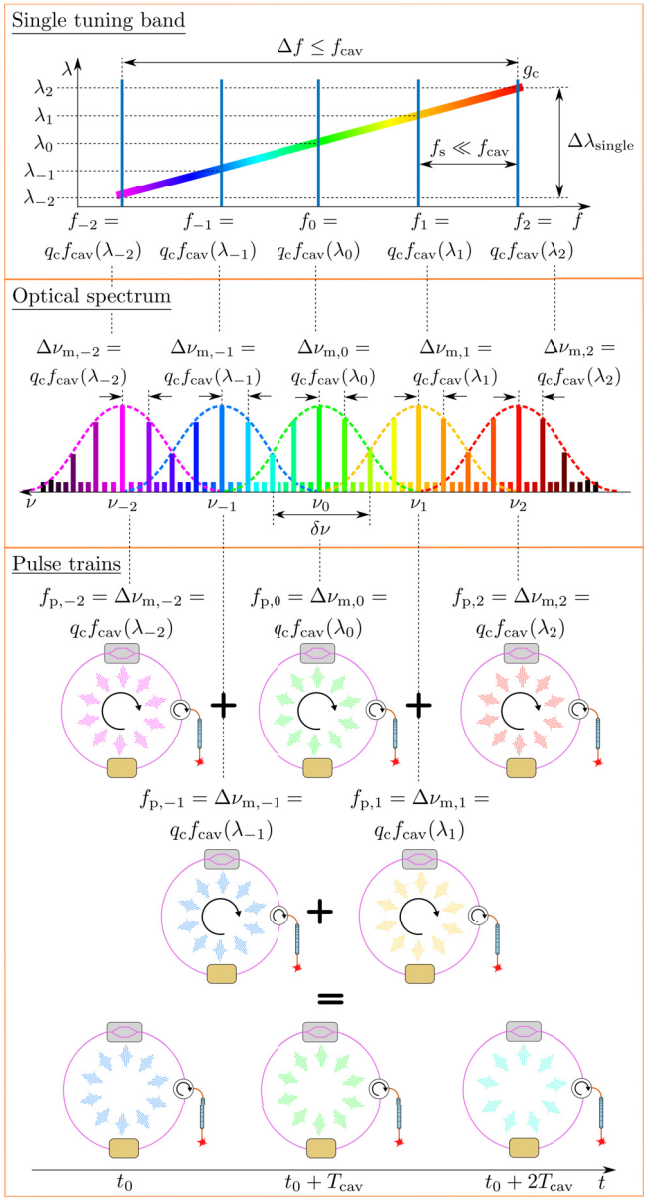

Fig. 6. Single-harmonic DTML. **Top:** Emission wavelength λ as a function of the modulation frequency f_l. **Middle:** Optical spectrum consisting of spectral lines at ν_l with an instantaneous linewidth of $\delta\nu = c\delta\lambda/\lambda^2$. **Bottom:** Monochromatic pulse trains with a carrier wavelength λ_l and a pulse rate given by $f_{\mathrm{p},l} = \Delta\nu_{\mathrm{m},l} = q_c f_{\mathrm{cav}}(\lambda_l)$, each corresponding to a single spectral line at ν_l in the spectrum from above.

wavelength operation tuning bandwidth $\Delta\lambda_{\text{single,n-d}}$ as:

$$\Delta\lambda_{\text{single,n-d}} \approx |S(f_0)|f_{\mathrm{cav}} = \frac{1}{|\mathrm{TDD}_{\mathrm{cav}}|f_0}. \tag{13}$$

Apparently, $\Delta\lambda_{\text{single,n-d}}$ reduces with f_0. However, it is advisable to find a trade-off between $\Delta\lambda_{\text{single,n-d}}$ and $S(f) \sim 1/f$, since with a small $S(f)$ the wavelength tuning is less sensitive to

Optics EXPRESS

instabilities in the modulation frequency $f(t)$ given by (1), which may lead to linewidth broadening [27].

The achievable tuning bandwidth is also affected by the sweep rate f_s, provided that the output power of the laser and its coherence should stay comparable to those achieved in the stationary regime (i.e., when $f_s = 0$). To examine the effects of fast tuning, the scaling guidelines developed in [34] can be adopted to DTML lasers as well [12,14], for the purposes of this study elaborated here in a more detail. A Fabry-Perót (FP) wavelength filter in [34] is replaced in a DTML laser by a combination of a cFBG with an intensity modulator. The spectral selection in a DTML laser achieved by a combination of a cFBG with an intensity modulator can be assimilated with the operation of an FP filter, with a spectral bandwidth of the FP filter replaced by the stationary regime linewidth $\delta\lambda_{\text{stat}}$ measured on an optical spectrum analyzer. In general, according to the predictions in [15,31–33], the larger anomalous dispersion in the cavity ($\gtrsim$ 10 ps/nm), combined with the narrower temporal modulation window ($\lesssim$ 100 ps), the smaller values of $\delta\lambda_{\text{stat}}$ are obtainable. A high anomalous dispersion enhances wavelength selectivity, while a narrow temporal modulation window better suppresses the amplified spontaneous emission (ASE) inside the cavity. When the modulation frequency is swept within a single qth band in the single-harmonic case, the filtered wavelength is tuned correspondingly, as outlined in the top panel of Fig. 7. $\Delta\lambda_{\text{round}}$ in the figure represents an average wavelength shift per round trip time $T_{\text{cav}} = 1/f_{\text{cav}}$. Figure 7 displays the wavelength filtering over a span of a few T_{cav} periods only.

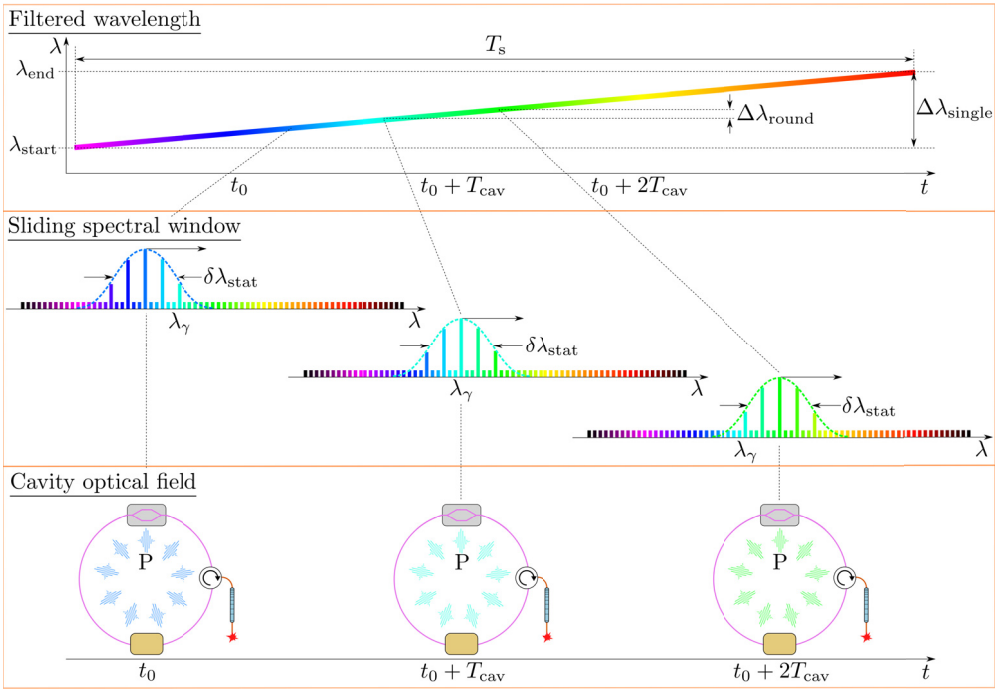

Fig. 7. Spectral filtering behavior in the single-harmonic DTML regime. **Top:** Filtered wavelength as a function of time. Each cavity round trip time T_{cav}, the filtered wavelength is tuned by $\Delta\lambda_{\text{round}}$. **Middle:** Snapshots of the sliding spectral window separated in time by T_{cav}. The window filters only the modes mode-locked in Fig. 6. $\delta\lambda_{\text{stat}}$ is the bandwidth of the filter and λ_γ is the wavelength of a photon γ circulating inside the cavity. **Bottom:** Snapshots of the cavity optical field separated in time by T_{cav}, with a specific pulse P circulating inside the cavity. The drawings are inspired by [20,34,35].

Optics EXPRESS

The prerequisite for saturated laser operation is that a photon γ of wavelength λ_γ circulating inside the cavity should complete on average at least R_{sat} round trips needed for gain saturation before its wavelength is outside of the spectral filtering window. This phenomenon is graphically depicted in the middle panel of Fig. 7, with the photon of wavelength λ_γ navigating inside the sliding spectral window of width $\delta\lambda_{\text{stat}}$. This imposes a limit on $\Delta\lambda_{\text{round}}$ in the form of:

$$\Delta\lambda_{\text{round}} \lesssim \frac{\delta\lambda_{\text{stat}}}{R_{\text{sat}}}. \tag{14}$$

Note that the sliding window in Fig. 7 operates on those modes which are mode-locked in Fig. 6 only. The carrier wavelength of a specific pulse P in the bottom panel of Fig. 7 matches the instantaneous filtered wavelength of the spectral window at the moment when the pulse passes through the modulator. Because the spectral window moves at a rate $f_s \ll f_{\text{cav}}$, only a fraction of the tuning bandwidth is stored inside the cavity at a time. R_{sat} in (14) can be estimated as [34]:

$$R_{\text{sat}} \approx \frac{\log\left(\frac{P_{\text{sat}}\Delta\lambda_{\text{SOA}}}{\delta\lambda_{\text{stat}}P_{\text{ASE}}}\right)}{\log[G_{\text{SOA}}(1-\rho_{\text{cav}})]}, \tag{15}$$

where P_{sat} is the saturation power, $\Delta\lambda_{\text{SOA}}$ is the gain bandwidth of the SOA, P_{ASE} is the total ASE power, G_{SOA} is the small signal gain, and ρ_{cav} represents all losses inside the cavity, including the output coupling. R_{sat} defined in (15) is a constant given by the cavity parameters, independent of the sweep frequency f_s. A maximum (single-harmonic) saturation operation tuning bandwidth limit $\Delta\lambda_{\text{single,sat}}$ can be estimated by substituting $\Delta\lambda_{\text{round}} \approx \Delta\lambda_{\text{single,sat}} f_s/f_{\text{cav}}$ in (14), where f_{cav}/f_s represents the total number of round trips needed for the carrier wavelength of the pulse P to be tuned from λ_{start} to λ_{end} in the single-harmonic DTML regime (assuming a linear wavelength tuning in the top panel of Fig. 7). By rearranging the terms in (14), the saturation operation tuning bandwidth limit $\Delta\lambda_{\text{single,sat}}$ for $|\Delta\lambda_{\text{single}}|$ is obtained as:

$$|\Delta\lambda_{\text{single}}| \lesssim \Delta\lambda_{\text{single,sat}} \approx \frac{\delta\lambda_{\text{stat}} f_{\text{cav}}}{R_{\text{sat}} f_s}. \tag{16}$$

The inequality in (16) provides a rough estimation for a maximum $|\Delta\lambda_{\text{single}}|$ below which the output power and coherence are expected to remain comparable to those achieved in the stationary regime. One way to increase the value on the right side is via shortening the cavity length that leads to increase in f_{cav}. However, this approach faces a technical limitation due to the nominal fiber length required for the cFBG [12,14]. This cavity length constraint, that ultimately limits the sweep rate and the achievable tuning bandwidth, is addressed by the long cavity multi-harmonic DTML discussed in the next section.

Another fast tuning limitation is obtained when a photon circulating inside the cavity completes on average only one round trip before its wavelength is outside of the sliding spectral window in the middle panel of Fig. 7. This imposes a limit on $\Delta\lambda_{\text{round}}$ in the form of:

$$\Delta\lambda_{\text{round}} \lesssim \delta\lambda_{\text{stat}}. \tag{17}$$

The maximum (single-harmonic) one round trip operation tuning bandwidth limit $\Delta\lambda_{\text{single,one}}$ can be estimated by substituting $\Delta\lambda_{\text{round}} \approx \Delta\lambda_{\text{single,one}} f_s/f_{\text{cav}}$ in (17). By rearranging the terms in (17), the one round trip operation tuning bandwidth limit $\Delta\lambda_{\text{single,one}}$ for $|\Delta\lambda_{\text{single}}|$ is obtained as:

$$|\Delta\lambda_{\text{single}}| \lesssim \Delta\lambda_{\text{single,one}} \approx \frac{\delta\lambda_{\text{stat}} f_{\text{cav}}}{f_s}. \tag{18}$$

Once the tuning bandwidth $|\Delta\lambda_{\text{single}}|$ is above the saturation limit $\Delta\lambda_{\text{single,sat}}$, given by (16), the output power and coherence begin to degrade more rapidly until the one round trip limit

Optics EXPRESS

$\Delta\lambda_{\text{single,one}}$, given by (18), is reached. Beyond this limit, the laser enters a free-running operation, where coherence is typically lost entirely. In the next section, the single-harmonic parameters $\Delta\lambda_{\text{single}}$, $\Delta\lambda_{\text{single,sat}}$, and $\Delta\lambda_{\text{single,one}}$ will be replaced by their multi-harmonic counterparts $\Delta\lambda_{\text{multi}}$, $\Delta\lambda_{\text{multi,sat}}$, and $\Delta\lambda_{\text{multi,one}}$, respectively.

2.2. Multi-harmonic DTML

2.2.1. Principle of wavelength tuning

As discussed in the previous section, fast sweeping in the single-harmonic DTML regime requires reduction of the cavity length to maintain $\Delta\lambda_{\text{single,sat}}$ and $\Delta\lambda_{\text{single,one}}$ given by (16) and (18) sufficiently large. This represents a technical limitation, as fiber components may not allow shortening the cavity below a few meters. This cavity length constraint is addressed in this section by employing a long cavity ($\sim 100 - 1000$ m) and introducing a different DTML regime: the multi-harmonic mode-locking. To examine the laser optical spectrum in this regime, the large number of sweep cycles framework will be exploited, developed in the previous section for the single-harmonic case. The basic concept of the multi-harmonic DTML is that the modulation frequency f in Fig. 3, satisfying the resonant condition given by (3), is not restricted to just a single tuning band q_c. To involve harmonic orders beyond q_c, two additional conditions are imposed on $f(t)$ (i.e., on the modulation signal $V(t)$). First, while (7)–9 remain valid, the sweep frequency is set close to the fundamental frequency of the cavity, $f_s \approx f_{cav}$. Therefore, the spacing f_s between the frequency components f_l in (10) is now much larger than in the single-harmonic case in Fig. 6, to the extent that each individual f_l corresponds to a separate tuning band $q_c + l$ (see the top panel of Fig. 8 and 9). To engage multiple tuning bands $q_c + l$, the modulation frequency range Δf is extended significantly, as shown in the top panels of Figs. 8 and 9, greatly exceeding the fundamental frequency of the cavity, $\Delta f \gg f_{cav} \approx f_s$. In this way, many tuning bands $q_c + l$ are involved in wavelength tuning. The total number of tuning bands Q involved is then estimated as:

$$Q \approx \frac{\Delta f}{f_s} + 1. \tag{19}$$

When the two multi-harmonic conditions, i.e., $f_s \approx f_{cav}$ and $\Delta f \gg f_{cav}$, are accomplished, wavelength tuning can be experimentally observed only if f_s is slightly detuned from the reference $f_{cav}(\lambda_0)$. Also, it is observed that the tuning bandwidth increases linearly with this detuning. An approximate formula for this dependency was proposed in [19], and its more general form applicable to any large Δf will be derived in this study.

For convenience, f_s can be expressed in the form:

$$f_s = f_{cav}(\lambda_0) + \delta f_s, \tag{20}$$

where $f_{cav}(\lambda_0)$ is the fundamental frequency for the emission wavelength λ_0, and δf_s represents the sweep frequency detuning from $f_{cav}(\lambda_0)$. For the cavity to be mode-locked, the frequency components $f_l = f_0 + l f_s$, with the spacing f_s given by (20), has to satisfy the resonant condition according to (3),

$$f_l = f_0 + l f_s = q_c f_{cav}(\lambda_0) + l[f_{cav}(\lambda_0) + \delta f_s]. \tag{21}$$

If $\delta f_s = 0$, that is $f_s = f_{cav}(\lambda_0)$, each component f_l (vertical blue bars in the top panel of Fig. 8) corresponds to a single emission wavelength λ_0 from several tuning bands $q_c + l$,

$$f_l = (q_c + l) f_{cav}(\lambda_0). \tag{22}$$

In this case, the optical spectrum in the middle panel of Fig. 8 consists of a single spectral line at an optical frequency $\nu_0 = c/\lambda_0$ with an instantaneous linewidth $\delta\nu = c\delta\lambda/\lambda^2$. This single line results from a superposition of lines at the same optical frequency ν_0, but with modes locked at

Optics EXPRESS

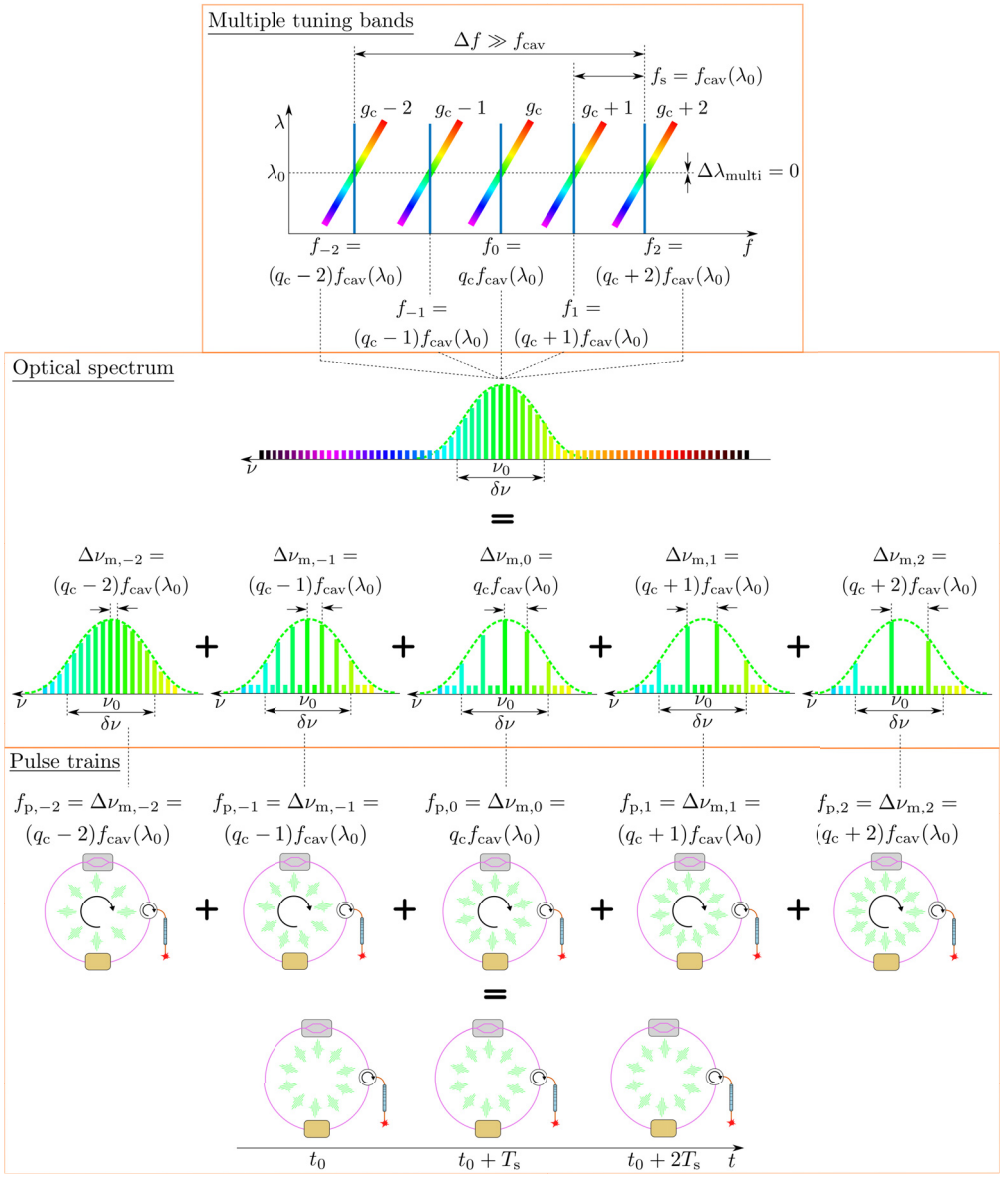

Fig. 8. Multi-harmonic DTML for the case $f_{\mathrm{s}} = f_{\mathrm{cav}}(\lambda_0)$. **Top:** Emission wavelength λ as a function of the modulation frequency f_l. **Middle:** Optical spectrum consisting of a superposition of spectral lines at $\nu_0 = c/\lambda_0$ with an instantaneous linewidth of $\delta\nu = c\delta\lambda/\lambda^2$, with different mode spacing given by $\Delta\nu_{\mathrm{m},l} = (q_{\mathrm{c}}+l)f_{\mathrm{cav}}(\lambda_0)$. **Bottom:** Monochromatic pulse trains with a carrier wavelength λ_0 and a pulse rate given by $f_{\mathrm{p},l} = \Delta\nu_{\mathrm{m},l} = (q_{\mathrm{c}}+l)f_{\mathrm{cav}}(\lambda_0)$, each corresponding to the spectral line at ν_0 from above.

different $(q_{\mathrm{c}}+l)$th harmonic order with mode spacing given by $\Delta\nu_{\mathrm{m},l} = (q_{\mathrm{c}}+l)f_{\mathrm{cav}}(\lambda_0)$. Again, for the graphical purposes, the spectral lines in Figs. 8 and 9 are approximated by a Gaussian spectral line shape with a linewidth $\delta\nu$. Each group of modes with spacing $\Delta\nu_{\mathrm{m},l}$ represents the spectrum of a monochromatic pulse train with a carrier wavelength λ_0 and a pulse rate given by $f_{\mathrm{p},l} = \Delta\nu_{\mathrm{m},l} = (q_{\mathrm{c}}+l)f_{\mathrm{cav}}(\lambda_0)$, perpetually circulating inside the cavity, as depicted in the bottom panel of Fig. 8. Despite the modulation frequency being swept fast, only one emission

Optics EXPRESS

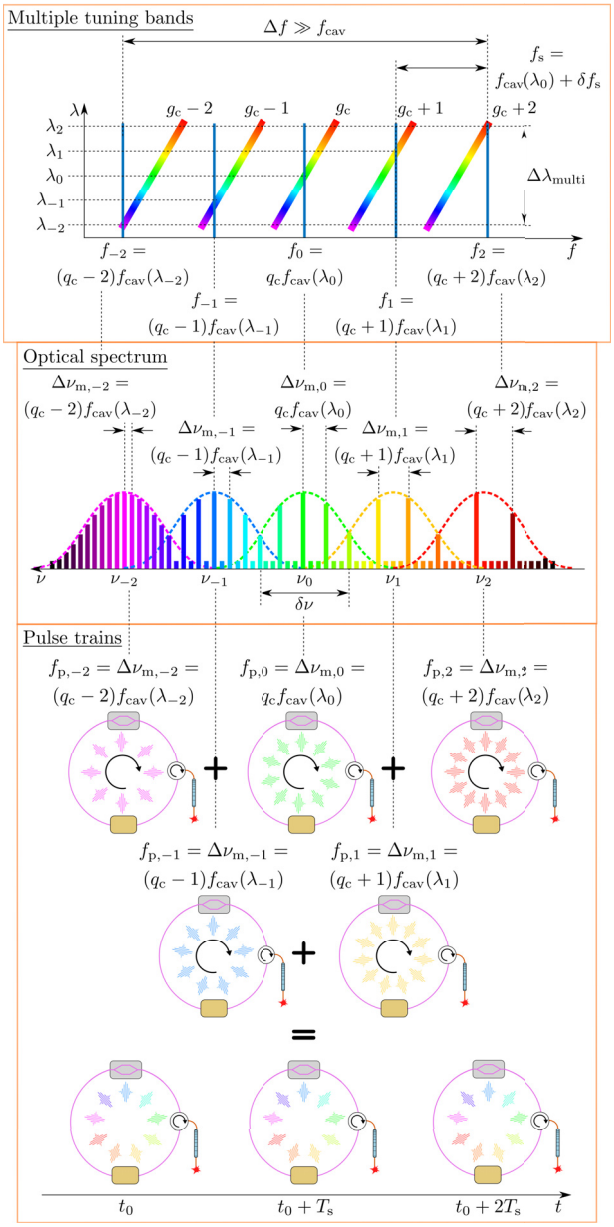

Fig. 9. Multi-harmonic DTML for the case $f_{\mathrm{s}} = f_{\mathrm{cav}}(\lambda_0) + \delta f_{\mathrm{s}}$. **Top:** Emission wavelength λ as a function of modulation frequency f_l. **Middle:** Optical spectrum consisting of several spectral lines at different optical frequencies $\nu_l = c/\lambda_l$ and an instantaneous linewidth of $\delta\nu = c\delta\lambda/\lambda^2$, with different mode spacing given by $\Delta\nu_{\mathrm{m},l} = (q_{\mathrm{c}} + l)f_{\mathrm{cav}}(\lambda_l)$. **Bottom:** Monochromatic pulse trains with a carrier wavelength λ_l and a pulse rate given by $f_{\mathrm{p},l} = \Delta\nu_{\mathrm{m},l} = (q_{\mathrm{c}} + l)f_{\mathrm{cav}}(\lambda_l)$, each corresponding to a spectral line at ν_l from above.

wavelength λ_0 is stored inside the cavity at a given time, similarly to the single-harmonic case for $f_{\mathrm{s}} = 0$, as displayed at the bottom of Fig. 8.

Optics EXPRESS

If $\delta f_s \neq 0$, each component f_l in (21) (vertical blue bars in the top panel of Fig. 9) corresponds to a different emission wavelength λ_l from several tuning bands $q_c + l$,

$$f_l = (q_c + l) f_{cav}(\lambda_l), \tag{23}$$

and a wavelength tuning takes place. In this case, the optical spectrum in the middle panel of Fig. 9 consists of several spectral lines at different optical frequencies ν_l. The modes within each line are locked at different $(q_c + l)$th harmonic order with spacing given by $\Delta\nu_{m,l} = (q_c + l) f_{cav}(\lambda_l)$. Each spectral line with modes spacing $\Delta\nu_{m,l}$ represents the spectrum of a monochromatic pulse train with a carrier wavelength λ_l and a pulse rate given by $f_{p,l} = \Delta\nu_{m,l} = (q_c + l) f_{cav}(\lambda_l)$, perpetually circulating inside the cavity, as depicted in the bottom panel of Fig. 9. A superposition of these monochromatic trains leads to a pulse train with a carrier wavelength varying over time, shown as snapshots of the optical field inside the cavity at periods of T_s in the bottom panel of Fig. 9.

In order to derive a quantitative formula for the tuning bandwidth $\Delta\lambda_{multi}$ in the multi-harmonic regime in Fig. 9, the same summing approach of fractional bandwidths $\Delta\lambda_{l+1,l} = \lambda_{l+1} - \lambda_l$ in (12) will be used. As the modulation frequency is now swept over a range of $\Delta f \gg f_{cav}$, $\Delta\lambda_{l+1,l}$ must be expressed as:

$$\begin{aligned} \Delta\lambda_{l+1,l} &\approx S\left(\frac{f_{l+1} - f_l}{2}\right)[f_{l+1} - f_l - f_{cav}(\lambda_0)] \\ &\approx S\left(\frac{f_{l+1} - f_l}{2}\right)\delta f_s, \end{aligned} \tag{24}$$

where $S((f_{l+1} - f_l)/2)$ denotes the average tuning sensitivity between the components f_{l+1} and f_l and where $\delta f_s = f_s - f_{cav}(\lambda_0) = f_{l+1} - f_l - f_{cav}(\lambda_0)$ (see the top panel of Fig. 9). $\Delta\lambda_{multi}$ is then given by a summation of all bandwidths $\Delta\lambda_{l+1,l}$:

$$\begin{aligned} \Delta\lambda_{multi} &\approx \sum_{l=-(Q-1)/2}^{(Q-1)/2-1} \Delta\lambda_{l+1,l} \\ &= \sum_{l=-(Q-1)/2}^{(Q-1)/2} S\left(\frac{f_{l+1} - f_l}{2}\right)\delta f_s, \end{aligned} \tag{25}$$

with the total number of tuning bands Q given by (19). Since the modulation signal comb-like spectrum in Fig. 5 consists usually of many components f_l, (25) can be further simplified by replacing the sum with an integral with $\mathrm{d}q$ as an infinitesimal variable. By evaluating the integral, a general formula for $\Delta\lambda_{multi}$ is obtained:

$$\begin{aligned} \Delta\lambda_{multi} &\approx \int_{-(Q-1)/2}^{(Q-1)/2-1} S(f)\delta f_s \mathrm{d}q \\ &= -\frac{\delta f_s}{\mathrm{TDD}_{cav} f_{cav}^2} \int_{f_0-\Delta f/2}^{f_0+\Delta f/2} \frac{\mathrm{d}f}{f} \\ &= -\frac{\delta f_s}{\mathrm{TDD}_{cav} f_{cav}^2} \ln\left(\frac{f_0 + \Delta f/2}{f_0 - \Delta f/2}\right), \end{aligned} \tag{26}$$

where $\mathrm{d}q = \mathrm{d}f/f_s \approx \mathrm{d}f/f_{cav}$ was used. Remarkably, $\Delta\lambda_{multi}$ is linearly proportional to δf_s. Considering for instance an anomalous dispersive cavity, i.e., when $\mathrm{TDD}_{cav}>0$, for $\Delta f>0$, the laser emission wavelength is tuned in the backward direction for $\delta f_s>0$, and in the forward

Optics EXPRESS

direction for $\delta f_s<0$. The tuning directions are reversed for $\Delta f<0$. (26) can be further summarized into a simpler linear relation:

$$\Delta\lambda_{\text{multi}} = S'_{\text{multi}}\delta f_s, \tag{27}$$

with S'_{multi} denoting the multi-harmonic tuning sensitivity, which generally depends on the cavity dispersion, its length, central modulation frequency f_0, and tuning range Δf. For $\Delta f/(2f_0) \ll 1$, (26) can be linearized in terms of Δf by first order expansion of the logarithm, leading to an approximative relationship, as already reported in [19]:

$$\Delta\lambda_{\text{multi}} \approx -\frac{\Delta f}{\text{TDD}_{\text{cav}} f_{\text{cav}}^2 f_0}\delta f_s. \tag{28}$$

2.2.2. Tuning bandwidth limitations

Similarly as in the single-harmonic case, the achievable tuning bandwidth $|\Delta\lambda_{\text{multi}}|$ in the multi-harmonic DTML is limited by several factors. The upper limiting factor without considering fast sweeping dynamic limitations is the gain bandwidth of the employed SOA and the bandwidths of the other cavity components. Another factor is due to the condition to prevent the laser from the undesired dual wavelength operation. Such a condition provides an estimation for the maximum non-dual wavelength operation multi-harmonic tuning bandwidth $\Delta\lambda_{\text{multi,n-d}}$. In analogy to (13), this can be estimated at the largest modulation frequency of the signal applied to the IM:

$$\Delta\lambda_{\text{multi,n-d}} = \frac{1}{|\text{TDD}_{\text{cav}}|(f_0 + \Delta f/2)}. \tag{29}$$

The achievable tuning bandwidth is further limited by the phenomena associated with the high speed of tuning, such as reduction of the output power and coherence length. To examine the multi-harmonic laser dynamic limitations, the scaling guidelines in [34] are adopted for the multi-harmonic DTML as well, with the combination of the cFBG and the IM operating as a tunable spectral filter. Figure 10 graphically depicts such wavelength filtering over a span of a few periods T_{cav}. Note that the sliding window in Fig. 10 operates on those modes which are mode-locked in Fig. 9 only. The carrier wavelength of a specific pulse P in the bottom panel of Fig. 10 matches the instantaneous filtered wavelength of the spectral window at the moment the pulse passes through the modulator. Because the spectral window moves at a rate of $f_s = f_{\text{cav}}(\lambda_0) + \delta f_s \approx f_{\text{cav}}$, the whole tuning bandwidth is stored within the cavity at any time. With the same reasoning leading to (14), the saturation laser operation imposes same limit on $\Delta\lambda_{\text{round}}$ in the top panel of Fig. 10. The maximum (multi-harmonic) saturation operation tuning bandwidth limit $\Delta\lambda_{\text{multi,sat}}$ can be estimated by substituting $\Delta\lambda_{\text{round}} \approx \Delta\lambda_{\text{multi,sat}} f_{\text{cav}}/|\delta f_s|$ in (14), where $f_{\text{cav}}/|\delta f_s|$ represents the total number of round trips needed for the carrier wavelength of the pulse P to be tuned from λ_{start} to λ_{end} in the multi-harmonic DTML regime (assuming a linear wavelength tuning in the top panel of Fig. 10). Rearranging the terms in (14), the saturation operation tuning bandwidth limit $\Delta\lambda_{\text{multi,sat}}$ for $|\Delta\lambda_{\text{multi}}|$ is obtained as:

$$|\Delta\lambda_{\text{multi}}| \lesssim \Delta\lambda_{\text{multi,sat}} \approx \frac{\delta\lambda_{\text{stat}} f_{\text{cav}}}{R_{\text{sat}}|\delta f_s|}. \tag{30}$$

However, as derived in (26), $\Delta\lambda_{\text{multi,sat}}$ and δf_s are not independent. By substituting for δf_s from (26) into (30) and rearranging it, the saturation operation bandwidth limit is obtained in the form:

$$\begin{aligned} |\Delta\lambda_{\text{multi}}| &\lesssim \Delta\lambda_{\text{multi,sat}} \\ &\approx \left[\frac{\delta\lambda_{\text{stat}}}{R_{\text{sat}}|\text{TDD}_{\text{cav}}|f_{\text{cav}}}\left|\ln\left(\frac{f_0 + \Delta f/2}{f_0 - \Delta f/2}\right)\right|\right]^{1/2}. \end{aligned} \tag{31}$$

The inequality in (31) provides a rough estimation for the maximum $|\Delta\lambda_{\text{multi}}|$ below which the output power and coherence performance are expected to remain comparable to those achieved

Optics EXPRESS

in the stationary regime. One way to increase the limit is by decreasing f_{cav} through extending the cavity length, while maintaining same $\text{TDD}_{\text{cav}} = D_{\text{fiber}}L_{\text{fiber}} + \text{TDD}_{\text{cFBG}}$ by employing a larger dispersion cFBG. However, this leads to a lower sweep rate, as given by $f_{\text{s}} \approx f_{\text{cav}}$ in the multi-harmonic regime. To raise the limit in (31) while preserving the sweep rate, an easy way would be to increase the logarithm, i.e., to increase Δf. Additionally, the limit can be also slightly raised by optimizing R_{sat}, given by (15), via reducing losses in the cavity by splicing the fiber components in Fig. 1, for instance.

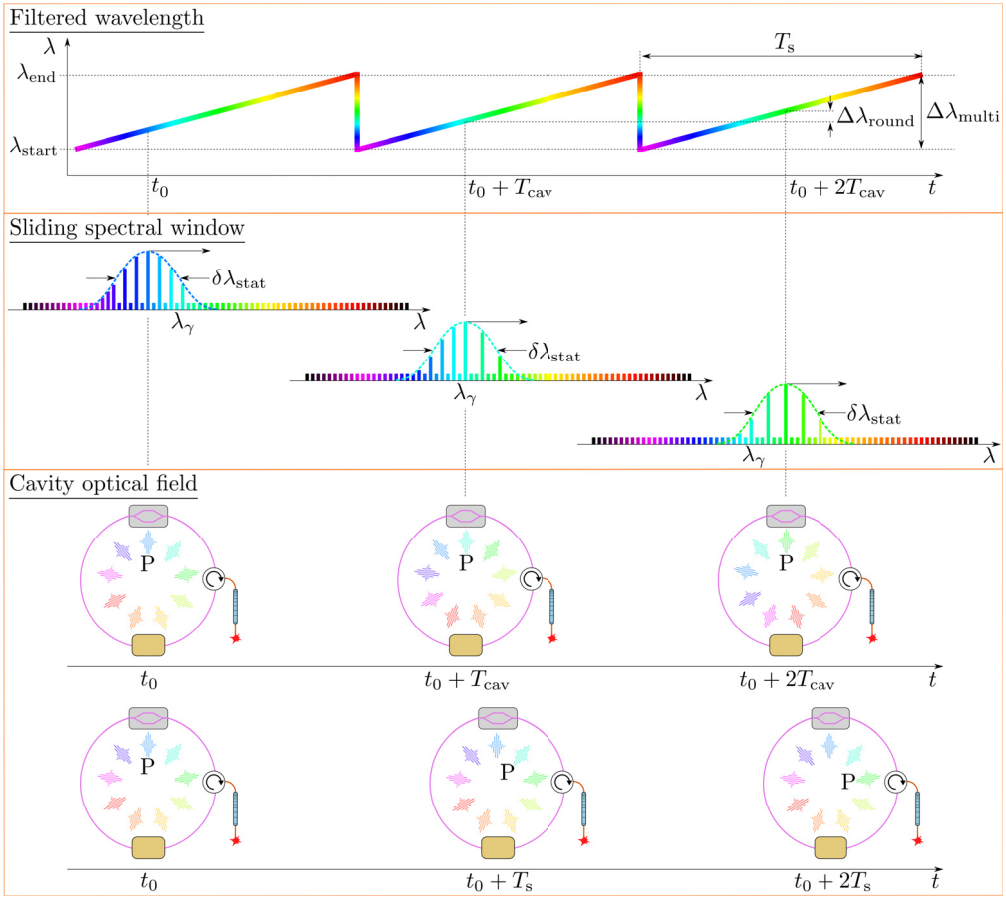

Fig. 10. Spectral filtering behavior in the multi-harmonic DTML regime. **Top:** Filtered wavelength as a function of time. Each cavity round trip time T_{cav}, the filtered wavelength is tuned by $\Delta\lambda_{\text{round}}$. **Middle:** Snapshots of the sliding spectral window separated in time by T_{cav}. The window filters only the modes mode-locked in Fig. 9. $\delta\lambda_{\text{stat}}$ is the bandwidth of the filter and λ_γ is the wavelength of a photon γ circulating inside the cavity. **Bottom:** Snapshots of the cavity optical field separated in time by T_{cav} and T_{s}, with a specific pulse P circulating inside the cavity. The drawings are inspired by [20,34,35].

Another bandwidth limit is obtained when a photon γ of wavelength λ_γ circulating inside the cavity completes on average only one round trip before its wavelength is outside of the sliding spectral window in the middle panel of Fig. 10. This imposes a limit on $\Delta\lambda_{\text{round}}$ in the form of (17). The maximum (multi-harmonic) one round trip operation tuning bandwidth limit $\Delta\lambda_{\text{multi,one}}$ can be estimated by substituting $\Delta\lambda_{\text{round}} \approx \Delta\lambda_{\text{multi,one}} f_{\text{cav}}/|\delta f_{\text{s}}|$ in (17). Rearranging the terms in (17), the one round trip operation tuning bandwidth limit $\Delta\lambda_{\text{multi,one}}$ for $|\Delta\lambda_{\text{multi}}|$ is

Optics EXPRESS

obtained as:

$$|\Delta\lambda_{\text{multi}}| \lesssim \Delta\lambda_{\text{multi,one}} \approx \left[\frac{\delta\lambda_{\text{stat}}}{|\text{TDD}_{\text{cav}}|f_{\text{cav}}}\left|\ln\left(\frac{f_0+\Delta f/2}{f_0-\Delta f/2}\right)\right|\right]^{1/2}. \tag{32}$$

To conclude the comparison between the single- and multi-harmonic DTML regimes, Table 1 lists side by side the main parameters and expressions characterizing their operations and tuning performances discussed in this study.

Table 1. Comparison of the main parameters and expressions characterizing the single- and multi-harmonic DTML regimes.

Parameter	Single-harmonic DTML	Multi-harmonic DTML
cavity length	$L_{\text{cav}} \lesssim 10$ m	$L_{\text{cav}} \sim 100-1000$ m
cavity dispersion	$\text{TDD}_{\text{cav}} \gtrsim 10$ ps/nm	$\text{TDD}_{\text{cav}} \gtrsim 10$ ps/nm
modulation frequency range	$\Delta f \leq f_{\text{cav}}$	$\Delta f \gg f_{\text{cav}}$
sweep rate	$f_{\text{s}} \ll f_{\text{cav}}$	$f_{\text{s}} \approx f_{\text{cav}}$
tuning bandwidth	$\lvert\Delta\lambda_{\text{single}}\rvert = \frac{1}{\lvert\text{TDD}_{\text{cav}}\rvert f_{\text{cav}} f_0}\lvert\Delta f\rvert$	$\lvert\Delta\lambda_{\text{multi}}\rvert = \frac{\lvert\delta f_{\text{s}}\rvert}{\lvert\text{TDD}_{\text{cav}}\rvert f_{\text{cav}}^2}\left\lvert\ln\left(\frac{f_0+\Delta f/2}{f_0-\Delta f/2}\right)\right\rvert$
saturation operation tuning bandwidth limit	$\Delta\lambda_{\text{single,sat}} \approx \frac{\delta\lambda_{\text{stat}} f_{\text{cav}}}{R_{\text{sat}} f_{\text{s}}}$	$\Delta\lambda_{\text{multi,sat}} \approx \left[\frac{\delta\lambda_{\text{stat}}}{R_{\text{sat}}\lvert\text{TDD}_{\text{cav}}\rvert f_{\text{cav}}}\left\lvert\ln\left(\frac{f_0+\Delta f/2}{f_0-\Delta f/2}\right)\right\rvert\right]^{1/2}$
one round trip operation tuning bandwidth limit	$\Delta\lambda_{\text{single,one}} \approx \frac{\delta\lambda_{\text{stat}} f_{\text{cav}}}{f_{\text{s}}}$	$\Delta\lambda_{\text{multi,one}} \approx \left[\frac{\delta\lambda_{\text{stat}}}{\lvert\text{TDD}_{\text{cav}}\rvert f_{\text{cav}}}\left\lvert\ln\left(\frac{f_0+\Delta f/2}{f_0-\Delta f/2}\right)\right\rvert\right]^{1/2}$

Table 2. Summary of the comparison of the key parameters and architectures between the multi-harmonic DTML and FDML. The information related to FDML lasers is primarily based on [35].

	Multi-harmonic DTML	FDML
cavity length	$L_{\text{cav}} \sim 100$ m	$L_{\text{cav}} \sim 100-1000$ m
tunable element	combination of a mode-locking with a dispersive element	Fabry-Perot tunable filter
cavity dispersion	$\text{TDD}_{\text{cav}} \gtrsim 10$ ps/nm	$\text{TDD}_{\text{cav}} \doteq 0$ ps/nm
synchronization with the cavity round trip time	slightly off	exactly synchronized
mode-locking orders	multiple	single
optical field	short pulses with a pulse rate given by the modulation frequency $f_{\text{p}} \approx f$	long pulses with a pulse rate comparable to the sweep frequency $f_{\text{p}} \sim f_s$
coherence length	units of millimeters	units of centimeters
sweep linearity	programmable sweep function	linear interval of a sinusoidal sweep function
dominant jitter source	RF source frequency/phase noise	FP filter synchronization
jitter tolerance	moderate (reasonable spectral purity of the RF source)	very low (picosecond-level synchronization)
cavity complexity	large modulation range Δf, polarization control	precise synchronization, dispersion compensation, polarization and temperature control, buffering

Optics EXPRESS

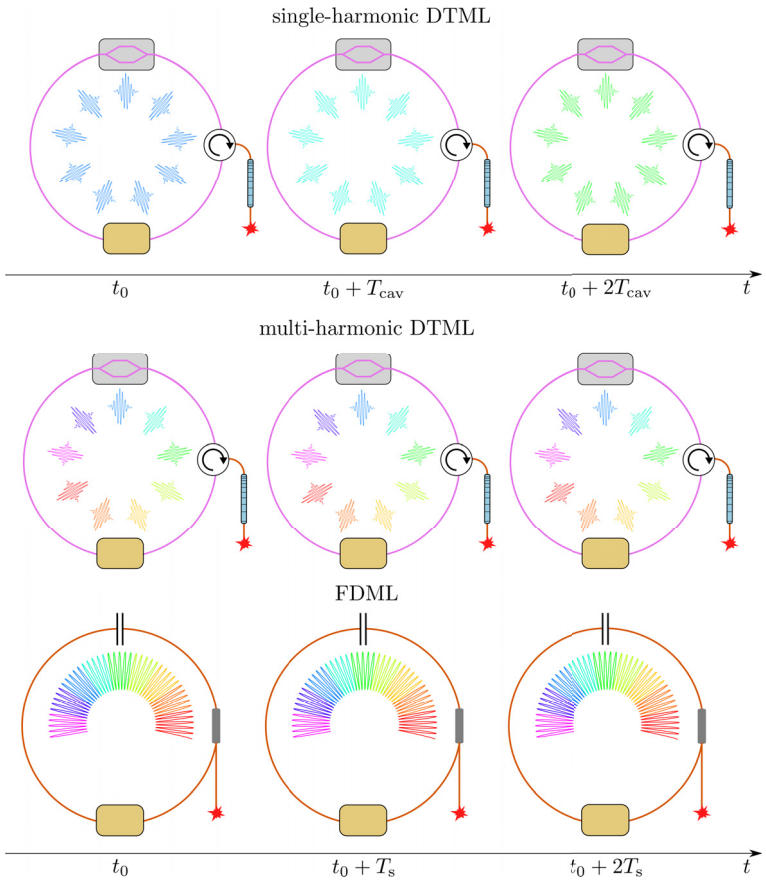

Fig. 11. A comparison of the optical fields stored inside a single-harmonic DTML, a multi-harmonic DTML, and an FDML cavity.

One prominent feature of the multi-harmonic tuning in Fig. 10 is that, because $f_s \approx f_{cav}$, the spectral window is tuned so fast that light (a photon γ of wavelength λ_γ), when arrives back at the modulator after a round trip inside the cavity, is filtered in the next tuning cycle (see the top panel in Fig. 10). This means that approximately $f_{cav}/|\delta f_s|$ tuning cycles are needed for the pulse P carrier wavelength to be tuned from λ_{start} to λ_{end}, unlike in the single-harmonic DTML in Fig. 6, where the light is filtered within a single tuning cycle. As the laser is tuned at a sweep rate close to the fundamental frequency of the cavity, the whole wavelength bandwidth is stored inside the cavity at any time. This feature makes the multi-harmonic DTML regime similar to a quasi-FDML operation [20,35]. A comparison of the optical fields stored inside a single-harmonic DTML, a multi-harmonic DTML, and an FDML cavity is graphically depicted in Fig. 11. However, some differences between the two regimes can be identified. First, the cFBG-modulator pair in the multi-harmonic DTML creates an akinetic spectral filter, while a mechanical tunable FP filter in FDML is employed. Second, as the mode-locking is achieved via the modulator, the optical field in a DTML cavity consists of short pulses with the repetition rate of the modulation frequency f, whereas optical field in an FDML cavity is in the form of long chirped pulses with a period comparable to T_s. Finally, a DTML cavity is inherently dispersive, inflicting a time delay between a pulse and the modulation window, needed for the wavelength tuning. This means that the number of round trips of a photon inside the cavity before it is blocked by the spectral filter decreases with increasing sweep rate. This is different from FDML,

Optics EXPRESS

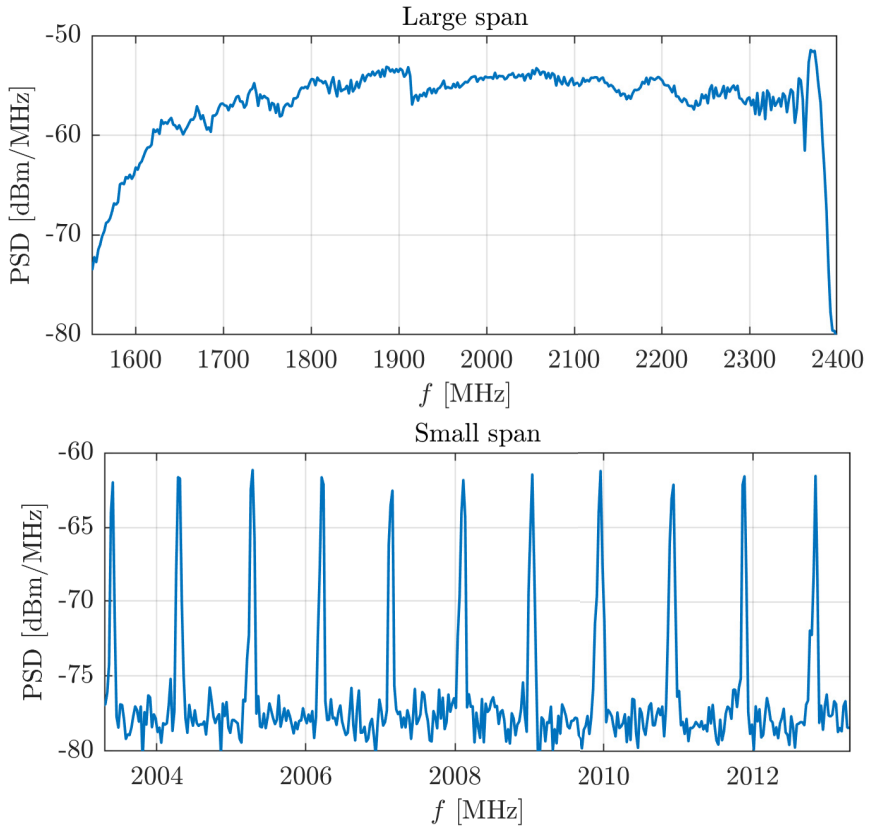

Fig. 12. Large span (top) and small span (bottom) of the VCO modulation signal spectral content applied to the IM in Fig. 1, with parameters $f_0 \doteq 2000$ MHz, $\Delta f \doteq 740$ MHz, and $f_s \doteq 0.944$ MHz.

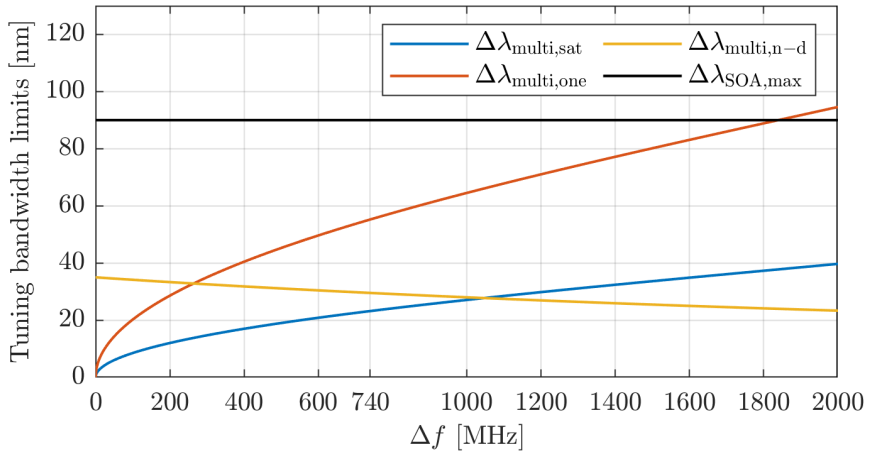

Fig. 13. Theoretical calculation of the tuning bandwidth limits $\Delta\lambda_{\text{multi,sat}}$, $\Delta\lambda_{\text{multi,one}}$, and $\Delta\lambda_{\text{multi,n-d}}$ using (31), (32), and (29), respectively, as a function of Δf. $\Delta\lambda_{\text{SOA,max}}$ is the maximum gain bandwidth of the employed SOA provided the maximum injection current is applied.

Optics EXPRESS

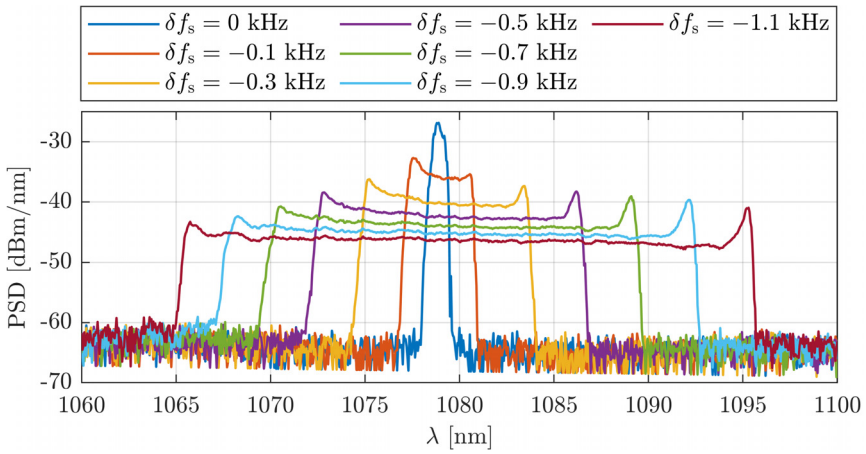

Fig. 14. Peak-hold optical spectra for various δf_s in (26). The measured tuning bandwidths as a function of δf_s are plotted in Fig. 15.

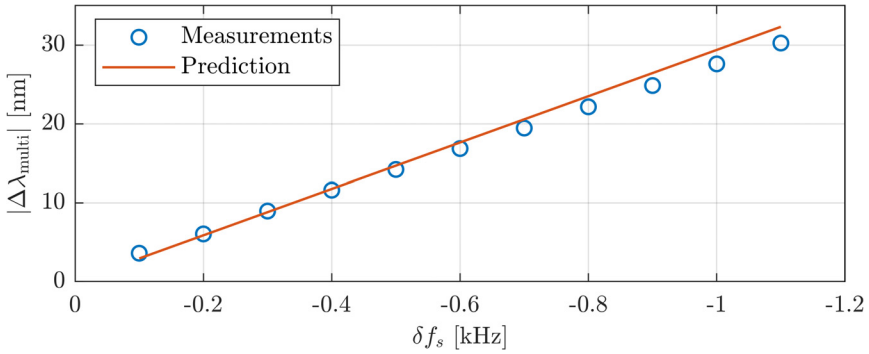

Fig. 15. Measured tuning bandwidths $|\Delta\lambda_{multi}|$ of the spectra in Fig. 14 and the theoretical prediction according to (26) as a function of δf_s.

where, if dispersion is well compensated, a large number of round trips for a photon is achieved. This drawback is to some extent compensated by a low complexity and much lower cost of a multi-harmonic DTML cavity in comparison to an FDML cavity, where dispersion must be accurately brought to zero. In DTML, on the other hand, dispersion in the cavity is necessary for the wavelength tuning, but its value does not have to be accurately managed (as long as it is $\gtrsim$ 10 ps/nm). In addition, DTML can exhibit linear-in-wavenumber sweeping by tailoring the voltage signal applied to the VCO, and so eliminating the need for k-clock triggering or post-processing linearization procedures [14,30]. The comparison of the main parameters and terms between multi-harmonic DTML and FDML lasers is summarized in Table 2.

3. Experimental results

The multi-harmonic DTML-SS in Fig. 1 was employed in the OCT setup in Fig. 2. The VCO modulation signal spectral content used for mode-locking of the laser is displayed in Fig. 12. The modulation frequency f was swept approximately linearly using a negative saw-tooth wave shape of $V_{AC}(t)$ at a sweep rate of $f_s \approx f_{cav} \doteq 0.944$ MHz over a $\Delta f \doteq 740$ MHz frequency range, and centered around the offset frequency of $f_0 \doteq 2000$ MHz. The spectrum contains approximately $\Delta f / f_s \doteq 780$ frequency components. Any noise on the input of the VCO is translated into

Optics EXPRESS

instabilities in the modulation frequency, therefore a low pass filter was employed, which however also reduced the maximum voltage that could be applied from the SG to the VCO in the setup in Fig. 1.

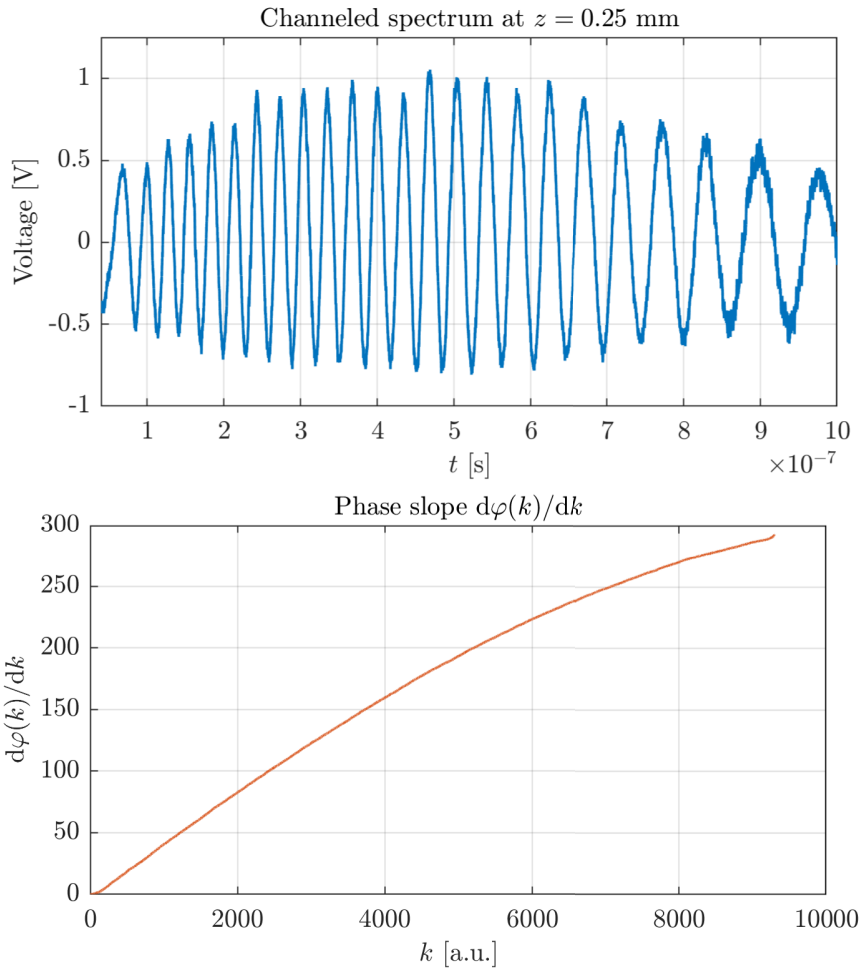

Fig. 16. Top: Photodetected signal showing the channeled spectrum for a mirror M used as the sample in Fig. 2 at the reference arm displacement z = 0.25 mm, obtained with a tuning bandwidth of $|\Delta\lambda_{\mathrm{multi}}| \doteq 30$ nm. **Bottom:** The extracted phase slope (group delay) $\mathrm{d}\varphi(k)/\mathrm{d}k$ as a function of wavenumber k using the CLF method.

An average stationary regime linewidth $\delta\lambda_{\mathrm{stat}} \doteq 0.11$ nm was measured on the optical spectrum analyzer. By substituting the measured parameters $P_{\mathrm{sat}} \doteq 31$ mW, $\Delta\lambda_{\mathrm{SOA}} \doteq 60$ nm (for the SOA injection current of 220 mA), $P_{\mathrm{ASE}} \doteq 2.75$ mW, $G_{\mathrm{SOA}} \doteq 1000$, and $\rho_{\mathrm{cav}} \doteq 0.995$ into (15), $R_{\mathrm{sat}} \doteq 5.7$ was calculated. Although injection current larger than 220 mA could be applied to extend the SOA gain bandwidth up to $\Delta\lambda_{\mathrm{SOA,max}} = 90$ nm (as seen in Fig. 13), increasing the current also led to a significant rise in ASE. To maintain acceptable noise performance, we limited the drive current to 220 mA, resulting in a bandwidth of approximately $\Delta\lambda_{\mathrm{SOA}} = 60$ nm. Figure 13 displays a theoretical calculation of bandwidths $\Delta\lambda_{\mathrm{multi,sat}}$, $\Delta\lambda_{\mathrm{multi,one}}$, and $\Delta\lambda_{\mathrm{multi,n\text{-}d}}$ using (31), (32), and (29), respectively, as a function of Δf, with specific values of $\Delta\lambda_{\mathrm{multi,sat}} \doteq 23$ nm, $\Delta\lambda_{\mathrm{multi,one}} \doteq 55$ nm, and $\Delta\lambda_{\mathrm{multi,n\text{-}d}} \doteq 30$ nm at $\Delta f = 740$ MHz. For a moment, let us suppose that the the single-harmonic DTML was employed with a shortest cavity

Optics EXPRESS

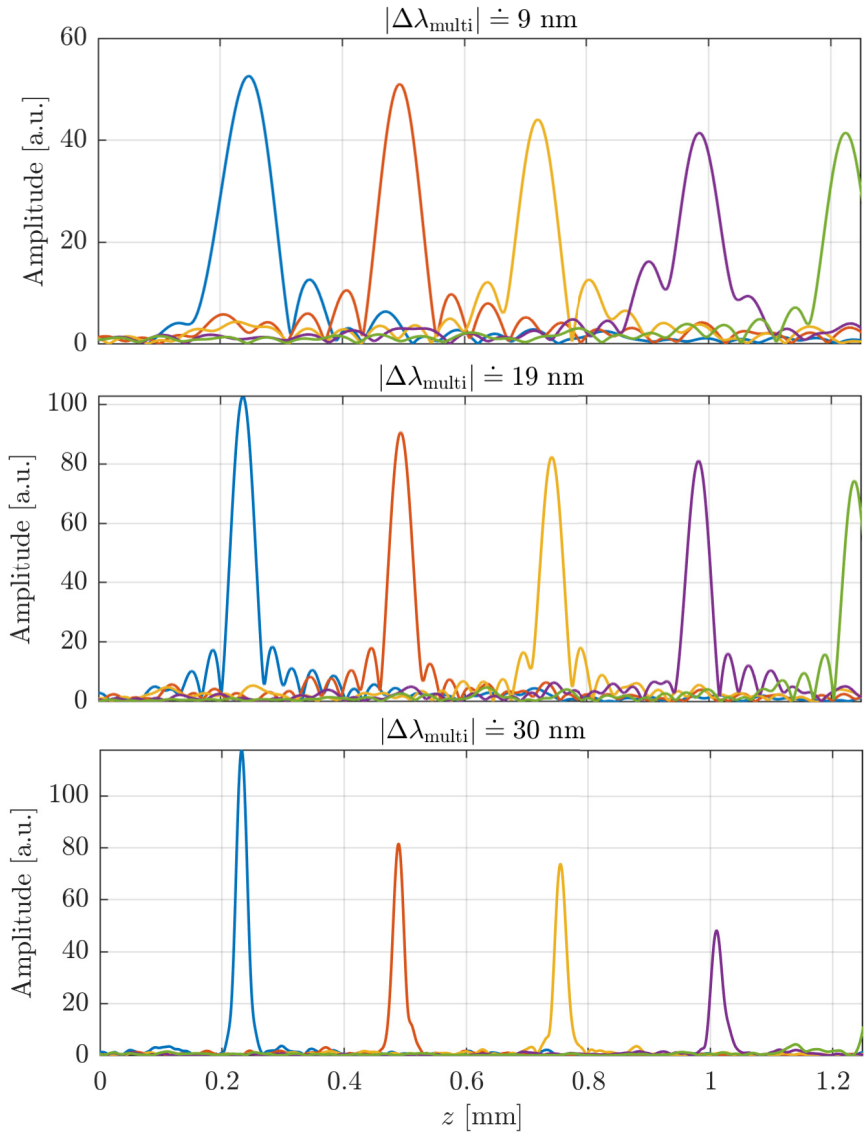

Fig. 17. Point spread functions roll-off measurements for three different tuning bandwidths $|\Delta\lambda_{\text{multi}}|$.

length of 1.542 m reported [12]. In this case, substituting $f_s = 0.944$ MHz, $\delta\lambda_{\text{stat}} = 0.11$ nm, and $R_{\text{sat}} \doteq 5.7$ in (16) and (18), limited bandwidths of $\Delta\lambda_{\text{single,sat}} \doteq 3$ nm (compare with $\Delta\lambda_{\text{multi,sat}} \doteq 23$ nm) and $\Delta\lambda_{\text{single,one}} \doteq 15$ nm (compare with $\Delta\lambda_{\text{multi,one}} \doteq 55$ nm) would be possible only.

Figure 14 shows peak-hold spectra of the laser under various detuning frequencies δf_s (without the BOA), with a central wavelength close to 1080 nm. The measured tuning bandwidths $|\Delta\lambda_{\text{multi}}|$ of the spectra in Fig. 15 increases linearly with $|\delta f_s|$, exhibiting a measured tuning sensitivity of $S'_{\text{multi}} \doteq 27.5$ nm/kHz, in good agreement with the prediction given by (26). Two types of drift were observed in the spectra in Fig. 14 during extended measurements. The first was a drift in the central wavelength λ_0, caused by a gradual shift in the central modulation frequency f_0. Since the system uses a VCO with a high tuning sensitivity η_{VCO}, even small shifts in the DC voltage V_{DC}

Optics EXPRESS

in (1) can lead to noticeable shift in the modulation frequency over time. To compensate for the drift in the central wavelength automatically, a feedback control scheme similar to that described in [14] could be implemented in future multi-harmonic DTML systems. The second type of drift originates from a shift in the bias point of the intensity modulator [36], which affects modulation depth and symmetry. This drift can be suppressed by employing an automatic bias control circuit. Both types of drift were observed to occur on a time scale of half an hour to units of hours.

To evaluate coherence properties of the swept source, a mirror M was used as a sample in the setup depicted in Fig. 2. The channeled spectrum resulting from interference at the reference arm displacement $z = 0.25$ mm is shown in the top graph of Fig. 16. To account for the chirp in the spectrum and produce A-scans, the method of Complex Leader-Follower (CLF) interferometry is employed [22–24]. Using the CLF method, the extracted phase slope (group delay) $\mathrm{d}\varphi(k)/\mathrm{d}k$ as a function of wavenumber k is displayed in the bottom graph of Fig. 16. This demonstrates that the multi-harmonic DTML-SS provides a continuous and monotonic wavelength tuning, despite involving many tuning bands in the top panel of Fig. 9. The channeled spectrum also exhibits a chirp requiring signal post-processing. Three sensitivity roll-off measurements for three different tuning bandwidths $|\Delta\lambda_{\mathrm{multi}}|$ as a function of z are displayed in Fig. 17. The measured DTML-SS output powers without the BOA, P_{out}, output powers after the BOA, P_{BOA}, and 50% sensitivity drop imaging depths, Δz, are listed in Tabe 3. In agreement with the estimated $\Delta\lambda_{\mathrm{multi,sat}} \doteq 23$ nm, the powers and coherence properties for $|\Delta\lambda_{\mathrm{multi}}| \doteq 9$ nm and 19 nm are comparable with the stationary regime $|\Delta\lambda_{\mathrm{multi}}| \doteq 0$ nm. For $|\Delta\lambda_{\mathrm{multi}}| \doteq 30$ nm, however, a more significant reduction in coherence is observed. For this tuning bandwidth, a sensitivity between 85 – 90 dB with 3.1 mW reference arm power and an axial resolution of 22 μm were measured at small z, which is in close agreement with the theoretical prediction $\approx 0.6\lambda^2/\Delta\lambda \doteq 23$ μm for a top-hat optical spectral shape [37].

Table 3. Measured output powers P_{out} and P_{BOA} and imaging depths Δz estimated by 50% sensitivity roll-off drops for three different tuning bandwidths $|\Delta\lambda_{\mathrm{multi}}|$. The imaging depth for $|\Delta\lambda_{\mathrm{multi}}| = 0$ nm was estimated using a single sided imaging depth expression $\Delta z \approx 0.22\lambda^2/\delta\lambda_{\mathrm{stat}}$ [35].

$\lvert\Delta\lambda_{\mathrm{multi}}\rvert$ [nm]	P_{out} [mW]	P_{BOA} [mW]	Δz [mm]
0	1.1	5.7	2.3
9	1.1	5.5	2
19	1	4.9	1.8
30	0.8	4.3	0.9

Using the setup in Fig. 2, with the swept source adjusted to a tuning bandwidth of 30 nm, B-scan OCT images of sweat ducts in a finger and the retina of a volunteer were captured in Fig. 18.

4. Conclusion

In this study, the first comprehensive theoretical model for the multi-harmonic DTML sweeping regime is presented. Although the approximative formula (28) for the tuning bandwidth $\Delta\lambda_{\mathrm{multi}}$ was already previously reported in [19], a more general expression (26) is here derived under the assumption that the modulation range Δf is comparable with the central frequency f_0, a common condition in the multi-harmonic DTML. The earlier expression (28) can be seen as a limiting case of (26) when $\Delta f \ll f_0$. The derivation of (26) is accompanied by a detailed analysis of the relationship between the spectral content of the modulation signal and the resulting optical spectrum of the laser. This relationship is illustrated graphically in Figs. 6, 8, and 9, alongside

Optics EXPRESS

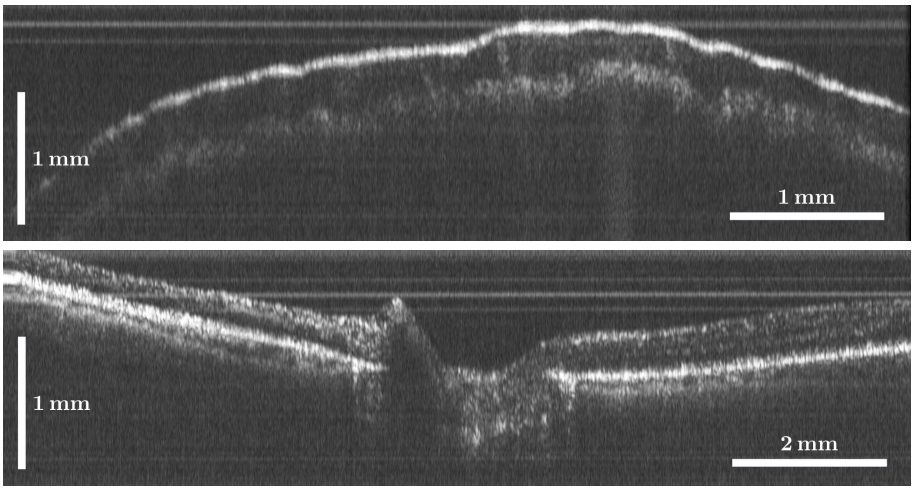

Fig. 18. B-scans captured with the setup in Fig. 2. **Top:** A finger tip. **Bottom:** Retina.

with an alternative time-domain interpretation based on monochromatic pulse trains circulating within the cavity. By incorporating the scaling guidelines outlined in [34], the dynamic tuning bandwidth limitations in (31) and (32) for the multi-harmonic regime are derived for the first time. The similarities and differences between the multi-harmonic DTML laser and both the single-harmonic DTML and FDML lasers are discussed in detail as well.

For the experimental validation of the regime, a swept source at 1 μm for OCT is demonstrated, exhibiting tuning over 30 nm bandwidth at nearly 1 MHz sweep rate. A 1 mm imaging depth is achieved and a sensitivity of up to 90 dB with 3.1 mW reference arm power is measured at a small z value. The first OCT images of a finger tip and the retina are captured employing a multi-harmonic DTML-SS. The apparent course for future research is to achieve wider tuning bandwidths while preserving the coherence properties of the laser.

To this end, the following optimization steps are proposed to improve the multi-harmonic DTML performance:

- Applying narrower modulation windows below 50 ps to achieve stronger ASE suppression, potentially improving the signal-to-noise ratio and coherence performance of the laser [15].
- Tolerating the dual-wavelength operation by employing Complex Leader-Follower (CLF) with stored channeled spectra, thereby removing the non-dual wavelength tuning bandwidth limit $\Delta\lambda_{\text{multi,n-d}}$ as given by (29).
- Employing a wider electrical bandwidth VCO or a scheme of grouping several VCOs, which could enlarge both $\Delta\lambda_{\text{multi,sat}}$ and $\Delta\lambda_{\text{multi,one}}$ (see Fig. 13).
- Assembling an all polarization maintaining (PM) architecture by identifying a manufacturer of PM-based cFBGs, which would eliminate the dependence of the central wavelength and the spectral modulation on polarization inside the cavity.
- Splicing fiber components together to reduce losses inside the cavity and lower R_{sat} as given by (15), and thereby extending $\Delta\lambda_{\text{multi,sat}}$ in accordance with (31).

The multi-harmonic DTML laser emerges as a promising fully akinetic, simple in design, low cost solution for megahertz SS-OCT applications.

Optics EXPRESS

Funding. Medical Research Council (662915, 18557, MR/X502753/1); European Commission (860807); National Institute for Health and Care Research (BRC4-05-RB413-302, NIHR202879); Biotechnology and Biological Sciences Research Council (BB/S016643/1, BB/X003744/1, BB/X511158/1); Engineering and Physical Sciences Research Council (EP/X000125/1).

Acknowledgments. The authors acknowledge support from the DPFS MRC (grant number 662915) awarded to the University of Nottingham and the University of Kent, and from the European Commission through the NETLAS ITN (grant agreement No. 860807). AP also acknowledges funding from the NIHR BRC4-05-RB413-302 at the UCL Institute of Ophthalmology and Moorfields Eye Hospital, as well as support from the NIHR202879 i4i Call 21. Additional funding was provided by the MRC Impact Acceleration Account (project 18557) and MR/X502753/1, the BBSRC grants BB/S016643/1, BB/X003744/1, and BB/X511158/1, including the University of Kent's BBSRC-funded Impact Acceleration Account. Further support came from the EPSRC (FoVEnOCT, EP/X000125/1) and the Imaging, Visual Assessment & Digital Innovation theme at Moorfields Eye Hospital NHS Foundation Trust and the UCL Institute of Ophthalmology.

Disclosures. AP is an inventor and co-inventor of patents in the name of the University of Kent.

Data availability. Data underlying the results presented in this paper are not publicly available at this time but may be obtained from the authors upon reasonable request.

References

1. D. Huang, E. Swanson, C. Lin, *et al.*, "Optical coherence tomography," Science **254**(5035), 1178–1181 (1991).
2. J. Fujimoto and W. Drexler, *Optical Coherence Tomography: Technology and Applications* (Springer Berlin Heidelberg, Berlin, Heidelberg, 2008).
3. T. Klein and R. Huber, "High-speed oct light sources and systems," Biomed. Opt. Express **8**(2), 828–859 (2017).
4. A. Martínez Jiménez, S. Grelet, V. Tsatourian, *et al.*, "400 hz volume rate swept-source optical coherence tomography at 1060 nm using a ktn deflector," IEEE Photonics Technol. Lett. **34**(23), 1277–1280 (2022).
5. M. Klufts, A. M. Jiménez, S. Lotz, *et al.*, "828 khz retinal imaging with an 840 nm fourier domain mode locked laser," Biomed. Opt. Express **14**(12), 6493–6508 (2023).
6. V.-F. Duma and A. G. Podoleanu, "Polygon mirror scanners in biomedical imaging: a review," in *Optical Components and Materials X*, vol. 8621 M. J. F. Digonnet, S. Jiang, and J. C. Dries, eds., International Society for Optics and Photonics (SPIE, 2013), p. 86210V.
7. J. Zhang, T. Nguyen, B. Potsaid, *et al.*, "Multi-mhz mems-vcsel swept-source optical coherence tomography for endoscopic structural and angiographic imaging with miniaturized brushless motor probes," Biomed. Opt. Express **12**(4), 2384–2403 (2021).
8. https://www.superlumdiodes.com/broadsweepers.htm,.
9. M. Bonesi, M. P. Minneman, J. Ensher, *et al.*, "Akinetic all-semiconductor programmable swept-source at 1550 nm and 1310 nm with centimeters coherence length," Opt. Express **22**(3), 2632–2655 (2014).
10. S. Grelet, A. M. Jimenez, P. B. Montague, *et al.*, "Shot-noise limited, 10 mhz swept-source optical coherence tomography for retinal imaging," IEEE Photonics J. **17**(2), 1–5 (2025).
11. T. S. Kim, J. Joo, I. Shin, *et al.*, "9.4 mhz a-line rate optical coherence tomography at 1300 nm using a wavelength-swept laser based on stretched-pulse active mode-locking," Sci. Rep. **10**(1), 9328 (2020).
12. H. D. Lee, G. H. Kim, J. G. Shin, *et al.*, "Akinetic swept-source optical coherence tomography based on a pulse-modulated active mode locking fiber laser for human retinal imaging," Sci. Rep. **8**(1), 17660 (2018).
13. S. Yamashita, N. Yuichi, K. Ryosei, *et al.*, "Wide and fast wavelength-swept fiber laser based on dispersion tuning for dynamic sensing," J. Sens. **2009**(1), 1 (2009).
14. H. D. Lee, M. Y. Jeong, C.-S. Kim, *et al.*, "Linearly wavenumber-swept active mode locking short-cavity fiber laser for in-vivo oct imaging," IEEE J. Sel. Top. Quantum Electron. **20**(5), 433–440 (2014).
15. H. Nagai and S. Yamashita, "Coherence improvement in dispersion-tuned swept laser by pulse modulation," Electron. Lett. **50**(23), 1729–1731 (2014).
16. R. Riha, A. M. Jimenez, G. Venugopal, *et al.*, "Dispersion-tuned mode-locked laser for swept source oct at 850 nm using a cfbg and the pulse modulation technique," IEEE Photonics J. **16**(4), 1–5 (2024).
17. F. Toadere, R.-F. Stancu, W. Poon, *et al.*, "1 mhz akinetic dispersive ring cavity swept source at 850 nm," IEEE Photonics Technol. Lett. **29**(11), 933–936 (2017).
18. R. F. Stancu and A. G. Podoleanu, "Dual-mode-locking mechanism for an akinetic dispersive ring cavity swept source," Opt. Lett. **40**(7), 1322–1325 (2015).
19. R. Riha, A. Bradu, and A. Podoleanu, "Dual resonance akinetic dispersive cavity swept source at 900 khz using a cfbg and an intensity modulator," Opt. Lett. **47**(16), 4032–4035 (2022).
20. R. Huber, M. Wojtkowski, and J. G. Fujimoto, "Fourier domain mode locking (fdml): A new laser operating regime and applications for optical coherence tomography," Opt. Express **14**(8), 3225–3237 (2006).
21. R. Riha and A. Podoleanu, "An approximative fiber laser cavity dispersion assessment technique using mode-locked wavelength tuning," in *Optical Coherence Tomography and Coherence Domain Optical Methods in Biomedicine XXVII*, (Optica, 2022), p. 512.
22. S. Rivet, M. Maria, A. Bradu, *et al.*, "Complex master slave interferometry," Opt. Express **24**(3), 2885–2904 (2016).

Optics EXPRESS

23. A. G. Podoleanu and A. Bradu, "Master–slave interferometry for parallel spectral domain interferometry sensing and versatile 3d optical coherence tomography," Opt. Express **21**(16), 19324–19338 (2013).
24. A. Bradu, S. Rivet, and A. Podoleanu, "Master/slave interferometry – ideal tool for coherence revival swept source optical coherence tomography," Biomed. Opt. Express **7**(7), 2453–2468 (2016).
25. U. Keller, *Ultrafast Lasers: A Comprehensive Introduction to Fundamental Principles with Practical Applications*, IOP Series in Coherent Sources, Quantum Fundamentals, and Applications (IOP Publishing, 2021).
26. C. Zhang, P. Liao, B. Burgoyne, *et al.*, "Low-cost dispersion-tuned active harmonic mode-locked laser with a 3-cm coherence length," IEEE J. Sel. Top. Quantum Electron. **20**(5), 399–405 (2014).
27. S. Yamashita and Y. W. Takubo, "Wide and fast wavelength-swept fiber lasers based on dispersion tuning and their application to optical coherence tomography," Photonic Sens. **3**(4), 320–331 (2013).
28. Y. Takubo and S. Yamashita, "High-speed dispersion-tuned wavelength-swept fiber laser using a reflective soa and a chirped fbg," Opt. Express **21**(4), 5130–5139 (2013).
29. H. D. Lee, J. H. Lee, M. Y. Jeong, *et al.*, "Characterization of wavelength-swept active mode locking fiber laser based on reflective semiconductor optical amplifier," Opt. Express **19**(15), 14586–14593 (2011).
30. H. Lee, G. H. Kim, M. Villiger, *et al.*, "Linear-in-wavenumber actively-mode-locked wavelength-swept laser," Opt. Lett. **45**(19), 5327–5330 (2020).
31. Y. Hasegawa, T. Shirahata, and S. Yamashita, "Analysis of dynamic properties of dispersion-tuned swept lasers," J. Lightwave Technol. **33**(1), 219–226 (2015).
32. A. Takada, M. Fujino, and S. Nagano, "Dispersion dependence of linewidth in actively mode-locked ring lasers," Opt. Express **20**(4), 4753–4762 (2012).
33. A. Takada, M. Saika, and S. Nagano, "Effect of linewidth enhancement factor in actively mode-locked ring laser," in *Fiber Lasers XI: Technology, Systems, and Applications*, vol. 8961 International Society for Optics and Photonics (SPIE, 2014), p. 896135.
34. R. Huber, M. Wojtkowski, K. Taira, *et al.*, "Amplified, frequency swept lasers for frequency domain reflectometry and oct imaging: design and scaling principles," Opt. Express **13**(9), 3513–3528 (2005).
35. R. Huber, "Fdml (incl. parallelization)," in *Optical Coherence Tomography*, W. Drexler and J. G. Fujimoto, eds. (Springer, Berlin, Heidelberg, 2015), pp. 741–787.
36. J. P. Salvestrini, L. Guilbert, M. Fontana, *et al.*, "Analysis and control of the dc drift in linbo3based mach-zehnder modulators," J. Lightwave Technol. **29**(10), 1522–1534 (2011).
37. J. P. Fingler, "Motion contrast using optical coherence tomography," Ph.D. thesis, California Institute of Technology (2007).